Development of a Coherent Optical Imaging System for Clinical Dermatology

by

Ahhyun Nam

B.S., Korea Advanced Institute of Science and Technology (2010)

Submitted to the Department of Mechanical Engineering
in partial fulfillment of the requirements for the degree of

Master of Science in Mechanical Engineering

at the

MASSACHUSETTS INSTITUTE OF TECHNOLOGY

June 2012

Author .....
Department of Mechanical Engineering
May 15, 2012

Certified by .....
Benjamin J. Vakoc
Assistant Professor of Dermatology
and Health Sciences and Technology, HMS, MGH
Thesis Supervisor

Certified by .....
George Barbastathis
Singapore Research Professor of Optics
and Professor of Mechanical Engineering
Thesis Reader

Accepted by .....
David E. Hardt
Chairman, Department Committee on Graduate Theses

Development of a Coherent Optical Imaging System for Clinical Dermatology

by

Ahhyun Nam

Submitted to the Department of Mechanical Engineering
on May 15, 2012, in partial fulfillment of the
requirements for the degree of
Master of Science in Mechanical Engineering

Abstract

The abnormal structure of cutaneous capillaries is associated with many skin diseases including skin cancer and port wine stain. Consequently, the demand for an imaging modality that can provide non-invasive visualization of capillary level blood flow is high. The major challenge in such imaging is to achieve high resolution and great flow sensitivity over a sufficient depth. Numerous imaging techniques derived from optical coherence tomography have provided a technical breakthrough and produced promising images of capillary networks of retina and brain tumors. However, these modalities have never been applied in clinical dermatological studies.

This thesis illustrates the process of design and complete construction of an optical frequency domain imaging (OFDI) system for dermal vasculature imaging that can be used in a clinical environment. The system consists of optical hardware, electronics, and a microscope; every part is contained in a portable cart that can be readily carried to a clinic. The optical subsystem includes a wavelength-swept laser source, a fiber optic interferometer with a delay stage and a polarization-sensitive balanced receiver. All power supplies, control drivers and monitoring circuits are integrated and enclosed in a case with a control interface. The microscope is attached to an articulating arm to be positioned as desired while the patient sits at ease.

The system performance is summarized as 10 μm resolution with frame rate of 100 frames per second. Further studies, in collaboration with dermatologists, will involve imaging the vascular structure of port wine stain lesions and investigating their correlation to laser treatment.

Thesis Supervisor: Benjamin J. Vakoc
Title: Assistant Professor of Dermatology
and Health Sciences and Technology, HMS, MGH

Acknowledgments

First of all, I would like to thank my advisor, Professor Benjamin J Vakoc, for his valuable advice and kind patience during my Master's program. I am truly grateful for his insightful guidance in academic works as well as for the great encouragement.

I would like to express my gratitude to all Vakoc group members, Nishant Mohan, Meena Siddiqui, and Ellen Zhang for helpful discussion and encouragement during my hard moments. I also am very grateful to Ashley Flibotte for her excellent administrative assistance.

I also wish to thank Professor William Wangyuhl Oh at KAIST, for being a great mentor to whom I can turn to at any times without having to prove myself.

It was a great pleasure to take the advanced workshop in writing with Jane Dunphy. Her guidance turned the thesis writing itself into a invaluable learning experience for me.

I want to thank Kwanjeong Educational Foundation of Korea and Wellman Center for Photomedicine for their generous support for the research.

Close friends have been with me through the highs and lows of the past two years. I am truly grateful for the support and friendship of Jiyoun Christina Chang, Uhirinn Suh, Taedong Yun, and Johnny Hyungruyl Choi. Very special thanks to Sungjune Bae for his sincere care and faithful love which made it possible for me to carry on trying after many downfalls.

Last but not least, my warmest regard and deepest love go to my family. My parents, Kichoon Nam and Haeyoung Hwang, have guided me to my present self with unconditional love. This work couldn't have been possible without their support. I would like to thank my not-so-little brothers, Kyuhyun and Junghyun, for heartwarming encouragement.

Contents

List of Figures

List of Tables

Chapter 1

Introduction

Non-invasive assessment of skin microvasculature is essential for diagnosis, treatment monitoring and pathological investigation in dermatology. Cutaneous microvascular structures are highly affected by skin cancers, as cancer cells induce angiogenesis to supply oxygen and nutrients. Capillary malformations result in pink or red lesions on the skin, and if formed in certain locations, can lead to glaucoma or Sturte-Weber syndrome. Dermal irritation, burn, and wound healing processes also involve injury and regeneration of blood vessels. As a result, the demand for an imaging modality that can provide non-invasive visualization of capillary level blood flow is very high.

The major challenge in microvasculature imaging is to achieve high resolution and great flow sensitivity over a sufficient depth. Specifically, microvessels are located in the dermis up to ~2 mm in depth, and their diameter measures ~10 μm. The flow velocity in capillary is as slow as ~0.5 mm/s at rest [1].

1.1 Related Works

During the past two decades, various derivatives of optical coherence tomography (OCT) have found applications in imaging blood flow. Early studies combined the concept of laser Doppler velocimetry with time domain OCT, which maps the Doppler frequency shift of the OCT signal that is caused by moving scatters in the blood [5, 8]. Here, the minimum detectable flow velocity was inversely coupled to the spatial res-

olution through the short time Fourier transform window. This undesirable coupling was eliminated by phase-resolved imaging techniques [22]. Phase-resolved time domain OCT(TD-OCT) determines the phase information by Hilbert transforming the TD-OCT signal and calculates the Doppler frequency shift from the phase information [21].

Frequency domain approaches brought significant advances in OCT imaging technology [10]. These approaches can be categorized in two different types: (1) the spectral domain approach where a broadband light source is used and the output signal is detected by a spectrometer and (2) the frequency domain approach where a wavelength-swept laser is used as a source and a single element photodiode as a detector [4]. These two approaches are also referred to as spectral domain OCT (SD-OCT) and optical frequency domain imaging (OFDI), respectively. Both types of imaging systems have been applied to imaging blood flow by mapping the phase shift of the interferometric output signal, and have shown promising images of human retina [23] and mouse brain tumor microvasculature (Figure 1-1-B) [16]. However, these phase resolved OCT techniques are highly sensitive to bulk tissue motion.

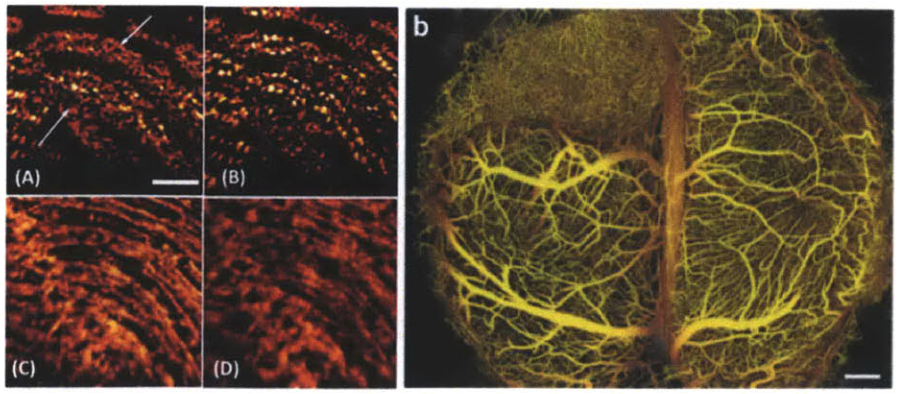

(A) (B)

Figure 1-1: Recent images of microvasculature obtained by (A) OMAG : images of human palm capillary networks in different depth (A-A) 400-450 μm, (A-B) 450-650 μm, (A-C) 650-780 μm, and (A-D) 780-1100 μm [1]; and (B) OFDI : images depth-projected vasculature within the first 2 mm of mouse brain tumor [16]

Optical micro angiography (OMAG) contrasts blood flow with static tissue by

processing a modulated spectral OCT signal. A piezoelectric scanner is added to the reference mirror of a conventional spectral domain OCT system. The modulated spectral interferogram undergoes a series of Hilbert and Fourier transforms after which the signals from the moving blood cells and the static tissue are separated into the positive and negative frequency space of fast Fourier transform (FFT) [17, 1].

Variance of speckle signals is also proved to provide blood flow contrast. This approach does not require any phase information. The speckle variance between the intensity image frames is larger in a static fluid than in a static tissue because of the Brownian motion of moving caterers in the fluid. This enables the mapping of the flow regardless of the Doppler angle, and can detect the capillaries that are parallel to the incident beam [12].

Interestingly, these OCT derived imaging modalities have not been applied to studies in clinical dermatology. Although the OMAG technique demonstrated promising preliminary images as shown Figure 1-1-A), the inherent complexity of the system has delayed its application in clinical studies.

1.2 Motivation

The main motivation of this thesis is to develop and construct an OFDI system for clinical studies of dermal microvasculature. Preliminary studies on a bench top system have been successful in imaging microvasculature of a mouse brain tumor. This study aims to build a clinical system that is specifically tailored for skin imaging based on the current laboratory system. A potential application of this study is to investigate vascular biology of port wine stain (PWS) in response to pulsed-dye laser (PDL) treatment.

1.2.1 Port Wine Stain (PWS)

PWS is a vascular birthmark that consists of dense and dilated capillaries in the skin. The name is derived from its reddish or purplish discoloration. The occurrence is approximately 0.3%, but the pathology is poorly understood. While benign, they

commonly present on the face and neck, and often cause measurable stress to children and young adults. As the discoloration does not fade over time, treatment is often recommended.

The most common method of PWS treatment employs a pulsed-dye laser to destroy excessive blood vessels. Laser pluses of wavelengths that match the absorption band of hemoglobin cause local heating within the vessel, and the heat causes thermal damage to the vessel. Current protocols use wavelengths from 577-600 nm and pulses with a duration ranging form 0.45-40 ms [14, 15]. While PDL therapy has proven beneficial to most patients, very few patients experience complete fading of the lesion. Additionally, as shown in Figure 1-2, some patients with initial improvement experience redarkening after a few years, whereas some patients do not respond to the therapy at all [7, 9]. Interesting to note is that it is not possible to predict the efficacy of the therapy before the treatment, and mechanisms underlying these poorly responding cases are unknown.

Figure 1-2: Redarkening of PWS after PDL treatment. Each panel shows a patient before treatment (left), after six treatments of PDL (middle), and at follow up examination after 9 years (Panel A) of 10 years (Panel B,C, and D). [7]

To improve the current therapy, we must first advance our understanding of underlying vascular biology of PWS treatment. Our OFDI system is expected to play a vital role in such clinical studies. Until now, there have been limited techniques to assess the vasculature before and after the treatment. Histological examinations

do not provide a non-invasive visualization of the vessels. Confocal microscopy provides *in vivo* imaging with fluorescent dyes but offers limited fields and penetration. A clinically deployable imaging system with capillary level high-resolution and sufficient penetration through the dermis would enable a better understanding of PWS physiology and improve the treatment.

1.3 Thesis Organization

Chapter 1 introduces the clinical motivation of this thesis regarding its application to study of port wine stain response to pulsed-dye laser therapy. The background study of optical coherence tomography (OCT) and optical frequency domain imaging (OFDI), the second-generation technology of the OCT, is covered in Chapter 2. The basic principles and theoretical performance limits of both techniques are explained. The detailed design and construction of the system is presented in Chapters 3 in the following order: the optical hardware; the electronics and control device; and the microscope interface. Chapter 4 evaluates system performance, presents a promising image of human dermal vasculature from the system, and concludes with the discussion of future work.

Chapter 2

Background

2.1 Optical Coherence Tomography

Optical coherence tomography (OCT) is an imaging modality derived from low coherence interferometry that can provide non-invasive high-resolution imaging of the subsurface structure of scattering materials. Figure 2-1 displays a schematic of a standard OCT system. A beamsplitter divides the incident light and directs it to the reference mirror and the sample. The reflected light from the reference mirror and the backscattered light from the sample recombine and interfere at the beamsplitter output.

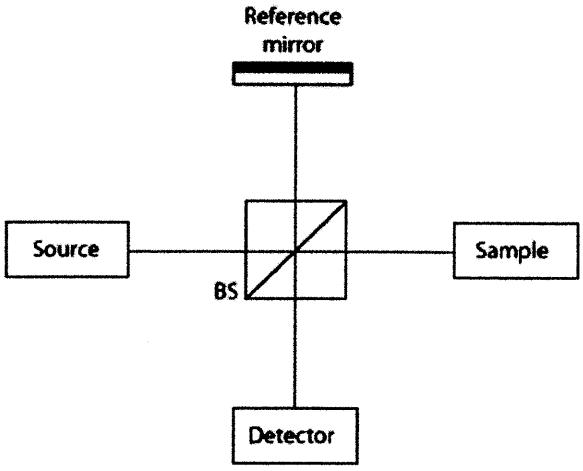

Figure 2-1: Schematic of OCT system. BS : Beamsplitter

Consider a simple case with a single mirror in the sample arm. If the source is monochromatic (coherent), the intensity of the recombined field output is proportional to the cosine of the optical path difference (OPD) Δl between the reference and the sample arms, as given by Equation 2.1.

$$I_o \sim |A_r|^2 + |A_s|^2 + 2A_r A_s \cos[k\Delta l(t)], \tag{2.1}$$

where $k = 2\pi/\lambda$ is the wavenumber; A_r and A_s are field amplitudes incident on the reference mirror and the sample mirror, respectively. However, if the source contains a spectrum of wavelengths or frequencies, the interference is observed only for the OPD values within the coherence length. The coherence length is inversely proportional to the source spectrum. OCT uses a broadband source (low coherence), because a short coherence length leads to the 'depth selection' ability. The peak value of the output envelope is proportional to the reflectivity of the sample at the certain depth of path-match. Hence, the reflectivity profile is obtained by scanning the reference mirror.

2.1.1 Performance Limits of OCT

As described in [2], the depth resolution of OCT imaging is directly related to the coherence length of the source and is inversely proportional to the source bandwidth. For a source with a Gaussian spectrum, the axial resolution δz is given by

$$\delta z = \frac{2\ln 2}{\pi}\left(\frac{\lambda_c^2}{n\Delta\lambda}\right), \tag{2.2}$$

where n is the refractive index of the sample, $\Delta\lambda$ is the full width at half maximum (FWHM) of the source power spectrum, and λ_c is the center wavelength of the spectrum. The transverse resolution of OCT imaging is defined as the minimum spot size of the sample beam, which is determined by the focusing property of the beam. The

transverse resolution δx is given by

$$\delta x = \frac{4\lambda}{\pi}\left(\frac{f}{d}\right) \tag{2.3}$$

where d is the beam diameter on the lens, and f is the focal length. A high numerical aperture (NA) results in a smaller spot size for the same beam, which leads to high transverse resolution. However, this high transverse resolution is achieved at the expense of reduced depth of focus , which is given by

$$b = \pi\frac{\delta x^2}{2\lambda}. \tag{2.4}$$

The depth of focus is interpreted as the depth in the sample that can be imaged, and is also referred to as the depth range. In OCT, the coherence gate decouples the axial resolution from the beam profile. Therefore, OCT imaging typically employs a low NA objective compared to confocal imaging, in order to achieve a large ranging depth.

2.1.2 Scanning Procedures and Image Display

To obtain three-dimensional information with OCT, it is necessary to implement the scanning mechanism in three directions. Depth scan, which is also called A-scan, in z direction is accomplished by scanning the reference mirror. Transverse scan, or B-scan, can be implemented either by a scanning mirror in the sample arm or translating the sample.

Different planes can be imaged with different scanning priorities of directions. The most common scanning method of OCT is the depth priority scan, which yields a tomographic imaging plane by measuring depth profiles at different lateral positions along a line. *En face* imaging is also possible by performing a two-dimensional transverse scan while holding the reference mirror fixed.

2.2 Optical Frequency Domain Imaging

Optical Frequency Domain Imaging (OFDI) is one of the two frequency domain alternatives for conventional (time domain) OCT. OFDI, like the other frequency domain alternatives, e.g. spectral domain OCT, enables much faster imaging with greater sensitivity by eliminating the need for scanning the reference mirror.

As discussed in [20], the principle of OFDI is based on optical frequency domain reflectometry (OFDR). Figure 2-2 shows the basic configuration of a fiber-based OFDR system. The source output splits into the reference and the sample arms. The interference is detected while the wavelength of a narrowband laser is swept while the reference mirror is fixed.

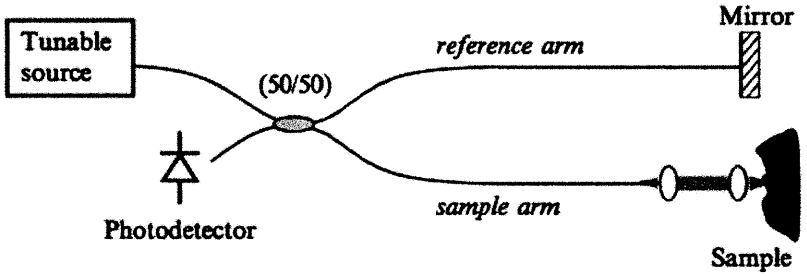

Figure 2-2: Basic configuration of OFDR system

The detector current is given by

$$i_{det}(t) = \frac{\eta q}{h\nu}\Big(P_r + P_s \int r^2(z)dz + 2\sqrt{P_r P_s}\int r(z)\Gamma(z)\cos\left(2k(t)z + \phi(z)\right)dz\Big), \quad (2.5)$$

where η is the detector sensitivity, q the quantum of electric charge (1.6×10^{-19} coulomb), $h\nu$ the single photon energy, P_r the optical power reflected from the reference arm, P_o the optical power illuminating the sample. The third term represents the interferometric signal, whereas the first and second terms contribute to the background. The coordinate z is defined along the depth into the sample where $z = 0$ is the path-match between the reference and the sample arm. $r(z)$ and $\phi(z)$ are the amplitude and the phase of the sample reflectivity at a depth z. $\Gamma(z)$ is the coherence function of the instantaneous laser output, and $k(t) = k_i + \alpha t$ is the wavenumber that

is varied monotonically over time t with a slope α.

If we consider, for simplicity, the case with a single reflector in the sample arm at $z = z_0$ where the input is considered coherent within the range that $\Gamma(z) = 1$, the signal current can be simplified:

$$i_{sig}(t) = \frac{\eta q}{h\nu} 2\sqrt{P_r P_s} r(z_0) \cos\left(2(k_i + \alpha t) z_0\right). \tag{2.6}$$

It is clear that the signal is proportional to the reflectivity $r(z_0)$, with the signal frequency in time ($\Omega = 2\alpha z_0$) encoding the depth z_0. Thus the depth reflectivity profile can be obtained by Fourier transforming the fringe signal, without having to scan the reference mirror.

2.2.1 Performance Limits of OFDI

The performance of OFDI is analyzed in the same way that conventional time domain OCT is analyzed. For a tuning source with a Gaussian-shaped spectrum, the axial resolution is given by [11]

$$\delta z = \frac{2\ln 2}{\pi} \left(\frac{\lambda_c^2}{n\Delta\lambda} \right), \tag{2.7}$$

which is the same as Equation 2.2. Likewise, the transverse resolution is governed by the beam profile, and given by the equation 2.3.

The depth range Δz is related to the sampling frequency of the digital acquisition (DAQ) board. According to the sampling theorem, the sampling frequency must be twice the maximum frequency of the signal from the maximum depth that can be imaged (Δz) in this case. The depth range is given by [6, 20]

$$\Delta z = \frac{\lambda_0^2}{4n\delta\lambda}, \tag{2.8}$$

where $\delta\lambda = \Delta\lambda / N_s$ is the sampling wavelength interval, and N_s is the number of samples within the FWHM of the spectrum $\Delta\lambda$. This sampling interval $\delta\lambda$ should be smaller than the instantaneous linewidth of the source in order to take advantage of the coherence of the narrowband. It is also shown in [20] that the signal-to-noise

ratio (SNR) of the OFDI system is improved to

$$(SNR)_{OFDI} = \frac{N_s}{2}(SNR)_{TD-OCT} \tag{2.9}$$

compared to the SNR of time domain OCT (TD-OCT).

2.2.2 Wavelength Swept Laser

As mentioned above, OFDI is operated by a tunable laser source with narrow linewidth. The laser characteristics that are most significant for OFDI can be summarized as the wavelength sweep range, the sweep repetition rate, and the instantaneous linewidth. The wavelength sweep range ($\Delta\lambda$) is related to the axial resolution (Δz), as can be seen in Equation 2.7. For imaging of a biological sample with a center wavelength at 1.3 μm, the scanning range has to be wider than 100nm in order to achieve the order of 10 μm resolution. The sweep repetition rate determines the imaging speed, since one sweep delivers one A-line profile. The instantaneous linewidth is relevant to the ranging depth in a way that the narrower the linewidth, the longer the coherence length that the signal from deeper point can be detected. An instantaneous linewidth of 0.1-0.2 nm is sufficient for many biomedical applications. [3]

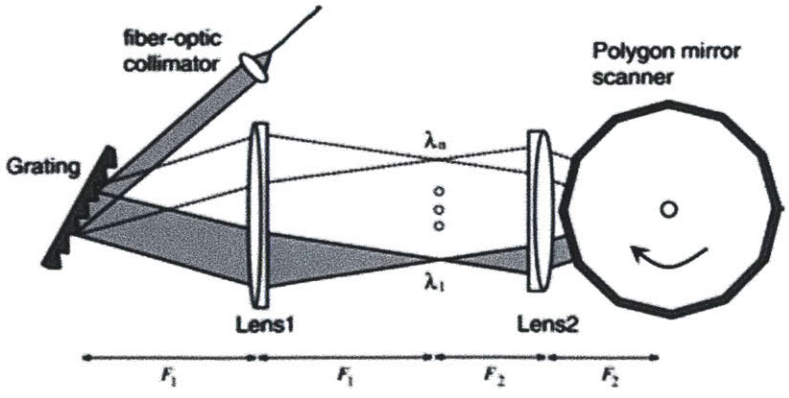

Figure 2-3: Schematic of polygon mirror based wavelength-scanning laser. [18]

One of the common implementations of this tunable laser source for OFDI systems is a semiconductor laser with a polygon mirror scanner and a diffraction grating

based wavelength-scanning filter [18]. Figure 2-3 presents the schematic of the filter. The reflection-type filter consists of three parts: a grating that splits the incident broadband light into narrowband wavelength components; an afocal telescope with two lenses that redirects the diverging beam from the grating to the polygonal mirror while controlling the beam diameter; and a polygonal scanner that reflects the narrowband component that is incident perpendicular to its facet.

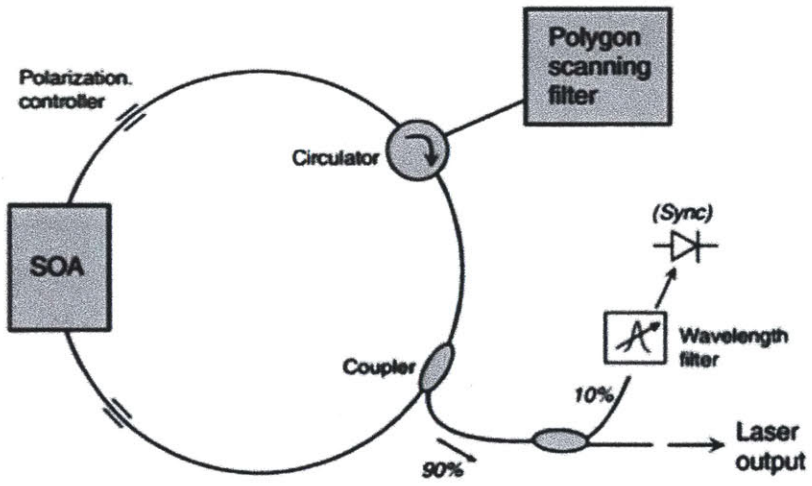

Figure 2-4: Schematic of the wavelength-scanning laser [18].

As illustrated in Figure 2-4, only the reflected wavelength component returns into a fiber-ring laser cavity, where it is amplified by a semiconductor optical amplifier (SOA). Rotation of the polygonal mirror sweeps the wavelength of the amplified output.

The equations of the parameters of this wavelength swept laser are summarized in Table 2.1. Note that a 100% duty cycle is achieved when all beams fall within a facet without clipping. The sweep range is determined by the free spectral range (FSR) of the laser. It has been demonstrated that the FSR can be twice as large when the wavelength-scanning filter is configured with an end reflector [13], as shown in Figure 2-5. This effect can be translated to a faster A-line rate by increasing the number of facets to $2N$ and keeping the same FSR.

Table 2.1: Important parameters of the wavelength swept laser

Diffraction wavelength	$\lambda = p(\sin\alpha + \sin\beta)$	p : grating pitch α : incident angle β : diffracted angle
Center wavelength	$\lambda_0 = p(\sin\alpha + \sin\beta_0)$	β_0 : angle between the optical axis and the grating normal
Free spectral range	$\Delta\lambda = p\cos\left(\frac{F_1}{F_2}\theta\right)$	F_1, F_2 : Focal lengths of the lenses
Instantaneous linewidth	$\delta\lambda = \sqrt{4\ln 2}\lambda_0 p\cos\alpha/(W\pi)$	W : $1/e^2$ beam width
Facet-to-facet polar angle	$\theta = 2\pi/N \approx L/R$	N : number of facets R : polygon diameter
Polygon facet width	$L = 2R\tan(\theta/2)$	
Beam width at polygon facet	$W' = WF_2\cos\beta/F_1\cos\alpha$	

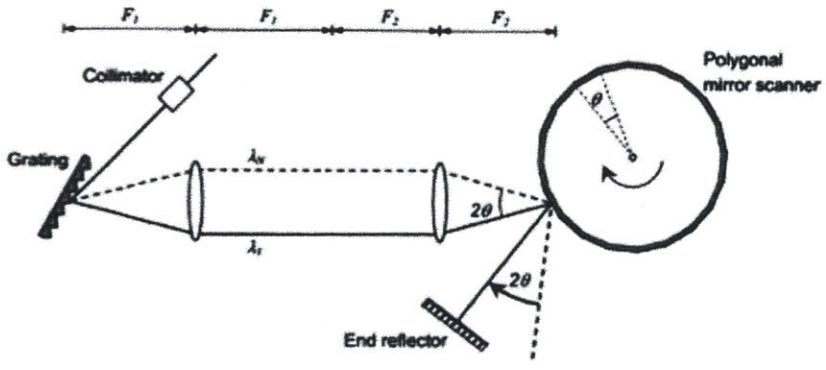

Figure 2-5: The configuration of the wavelength-scanning filter with an end reflector [13].

2.2.3 Optical Frequency Shifter

In OFDI, the ranging depth is limited by the coherence length of the instantaneous output of the wavelength swept laser. The fringe visibility decreases due to the finite extent of the coherence length, as seen by the term $\Gamma(r)$ in Equation 2.5. Moreover, the ranging depth is restrained by the inability to distinguish the positive and the negative frequency in an argument of a cosine function in Equations 2.5 and 2.6.

One approach to achieve the maximum raging depth within the coherence length is to use an optical frequency shifter in the interferometer to shift the frequency of the detector signal [19]. Figure 2-6 illustrates a schematic of an OFDI system with an optical frequency shifter.

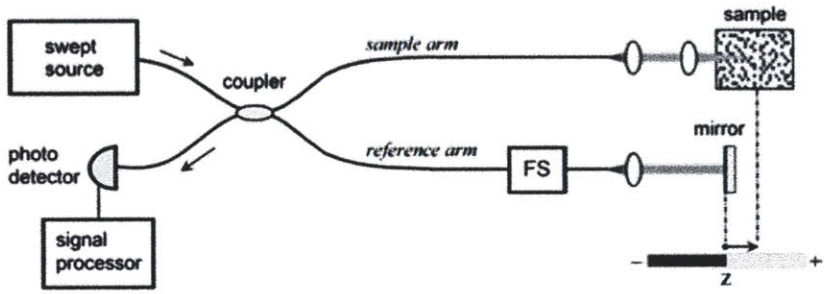

Figure 2-6: A basic configuration of an OFDI system with a frequency shifter FS : frequency shifter [19].

The signal current can be expressed as

$$i_{sig}(t) = \frac{\eta q}{h\nu} 2\sqrt{P_r P_s} \int r(z)\Gamma(|z|) \cos\left(2k(t)z + \phi(z) + 2\pi\Delta f t\right) dz\Big), \tag{2.10}$$

where Δf is the round-trip frequency shift. Note it is the third term in Equation 2.5 with the frequency shift term Δf. With a linear sweep in wavenumber, $k(t) = k_i + \alpha t$; then the detector signal frequency is given by

$$f_{sig} = \left|\frac{\alpha}{\pi} z + \Delta f\right|. \tag{2.11}$$

Therefore, as shown in Figure 2-7, now the negative frequency can be mapped in the positive frequency domain, shifted by Δf and both sides of the coherence range

can be used.

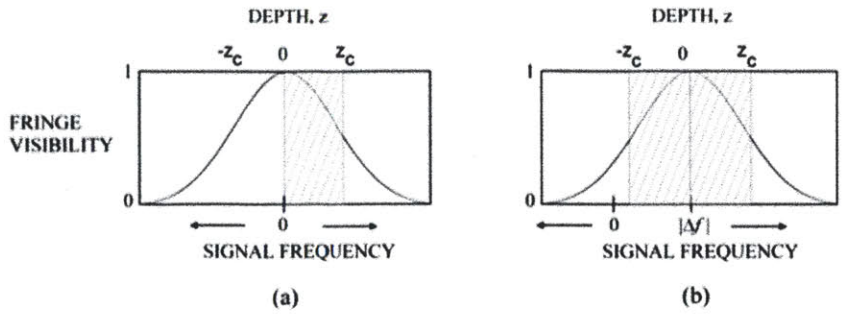

Figure 2-7: Illustration of the ranging depth (a) without and (b) with a frequency shifter [19].

2.2.4 Balanced Detection

As seen in Equation 2.1, the OCT signal comprises the background DC terms and the AC term that provides the sample information. Balanced receiver detects the oscillating term of the interferometric output by subtracting the quadrature signals of the beamsplitter. The quadratures can be detected because the transmitted field and the reflected field from the beamsplitter have a $\pi/2$ phase difference. Figure 2-8 illustrates a conceptual schematic of a balanced receiver.

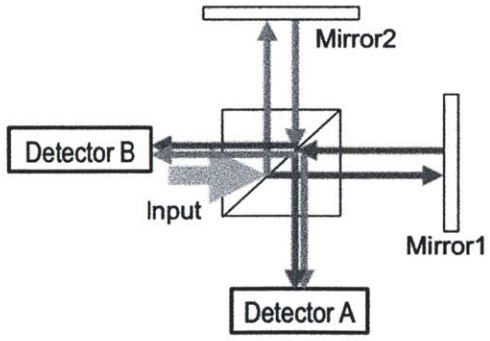

Figure 2-8: Schematic of a balanced receiver concept.

The intensities at Detectors A and B are given by the following:

$$I_A = |E_A|^2 = |iE_1 + iE2|^2 = E_1^2 + E_2^2 + 2\cos(2k\Delta l), \tag{2.12}$$

$$I_B = |E_B|^2 = |E_1 + i^2 E_2|^2 = E_1^2 + E_2^2 - 2\cos(2k\Delta l), \tag{2.13}$$

where E_A and E_B are the fields at each detector; E_1 and E_2 are the fields incident to mirrors 1 and 2 divided from the beamsplitter, represented by the orange and green colors, respectively; k is the wave number; and Δl is the OPD. The balanced detection is implemented by subtracting Equation 2.13 from Equation 2.12.

Chapter 3

System Design and Construction

This chapter describes the design and the construction of an OFDI system for dermal vasculature imaging that can be used in a clinical environment. The system consists of optical hardware, electronics, and a microscope. The whole systems is encased in a portable cart (61 cm×101.4 cm×92.9 cm, W×D×H) with a monitor and the microscope attached to it.

3.1 Optical Subsystem

There were three constraints in designing the optical hardware. First, to obtain images of capillary flow, it is necessary to achieve the performance of 5 μm resolution over a ranging depth of 3 mm. The source center wavelength was chosen to be 1300 nm, because it has low absorption in biological samples while penetrating to sufficient depth. To satisfy the specification with the chosen center wavelength, the source must be configured to achieve an FSR greater than 100 nm and a coherence length greater than 2 mm on both sides of the signal spectrum.The second constraint is the short imaging time imposed by the clinical environment. In this thesis, the imaging speed was aimed at 100 frames per second, which is equivalent to an A-line rate of 80 kHz. Last, all opto-mechanical components had to be confined to an optical breadboard of size 42 cm×66 cm. The breadboard was mounted on a sliding shelf in the cart. Optical fibers were laid out on a panel, which was fixed under the sliding shelf.

3.1.1 Optical Source : Short Cavity Wavelength Swept Laser

Conventional OFDI systems employ a fiber-ring cavity wavelength swept laser, which is illustrated in Section 2.2.2, Figure 2-4, where a narrow linewidth spectral filter is inside a fiber-ring cavity with a broadband gain medium. In order for one narrowband pulse to build up sufficient gain while maintaining the instantaneous linewidth and the sweep rate, the cavity length is must be as short as possible. For the desired sweep rate of 80 kHz, the total cavity length must be shorter than 2 m. However, due to the fiber length required by polarization controllers in the cavity, it was difficult to reduce the fiber length below the required level. The alternative approach was to replace the fiber coupler with a free-space beamsplitter. A schematic of this new set up is illustrated in Figure 3-1.

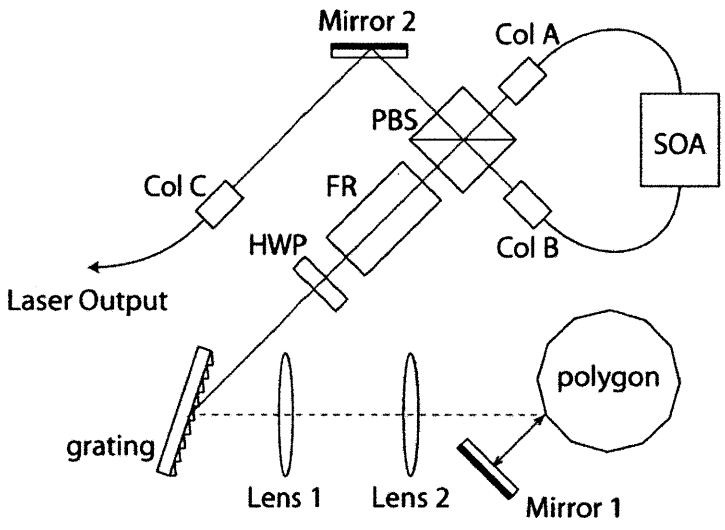

Figure 3-1: Schematic of the short cavity wavelength-scanning laser.
SOA : Semiconductor Optical Amplifier; PBS : Polarization beamsplitter; FR : Faraday rotator; HWP : Half wave plate; Col : Collimator

To ensure stability in the lasing direction, we used a polarization beamsplitter (PBS) with a Faraday rotator(FR) and a half-wave plate (HWP). Collimator A is configured so that the incident field is split into a 50/50 ratio at the PBS, while the first order diffraction is maximum at the grating so that power loss through grating is

minimum. The FR shifts the polarization by 45° in both directions of travel, whereas the HWP shifts 90° in one direction and reverses the shift to -90° in the opposition direction. Therefore, the polarization of the filter input field is perpendicular to the filter output; the output is directed to Collimator B. Collimator B is configured to have the maximum power from the transmission of the PBS, which is equivalent to the maximum coupling of the reflected output to the cavity.

As a result, the total cavity length including the double path within the filter is reduced from 3.4 m (fiber-ring) to 1.2 m. The alignment process is summarized in Appendix A

3.1.2 Interferometer

The system is based on a fiber-optic interferometer, which is more robust in terms of physical alignment. The schematic of the interferometer is provided in Figure 3-2.

To achieve a full ranging depth, an acoustooptical frequency shifter is inserted in the reference arm. The amount of optical frequency shift Δf was calculated from

$$\Delta f = \frac{f_{samp}}{4}, \tag{3.1}$$

where f_{samp} is the sampling frequency of the data acquisition (DAQ) instrument.

Note we implemented a mirror to calibrate the signal in the post-processing process. This calibration compensates for the nonlinearity of the sampling as well as dispersion. A computer-controlled shutter is implemented to block the light from the calibration mirror during the imaging process. The calibration mirror and the reference mirror are fixed on a motorized delay stage. The alignment process is explained in Appendix B.

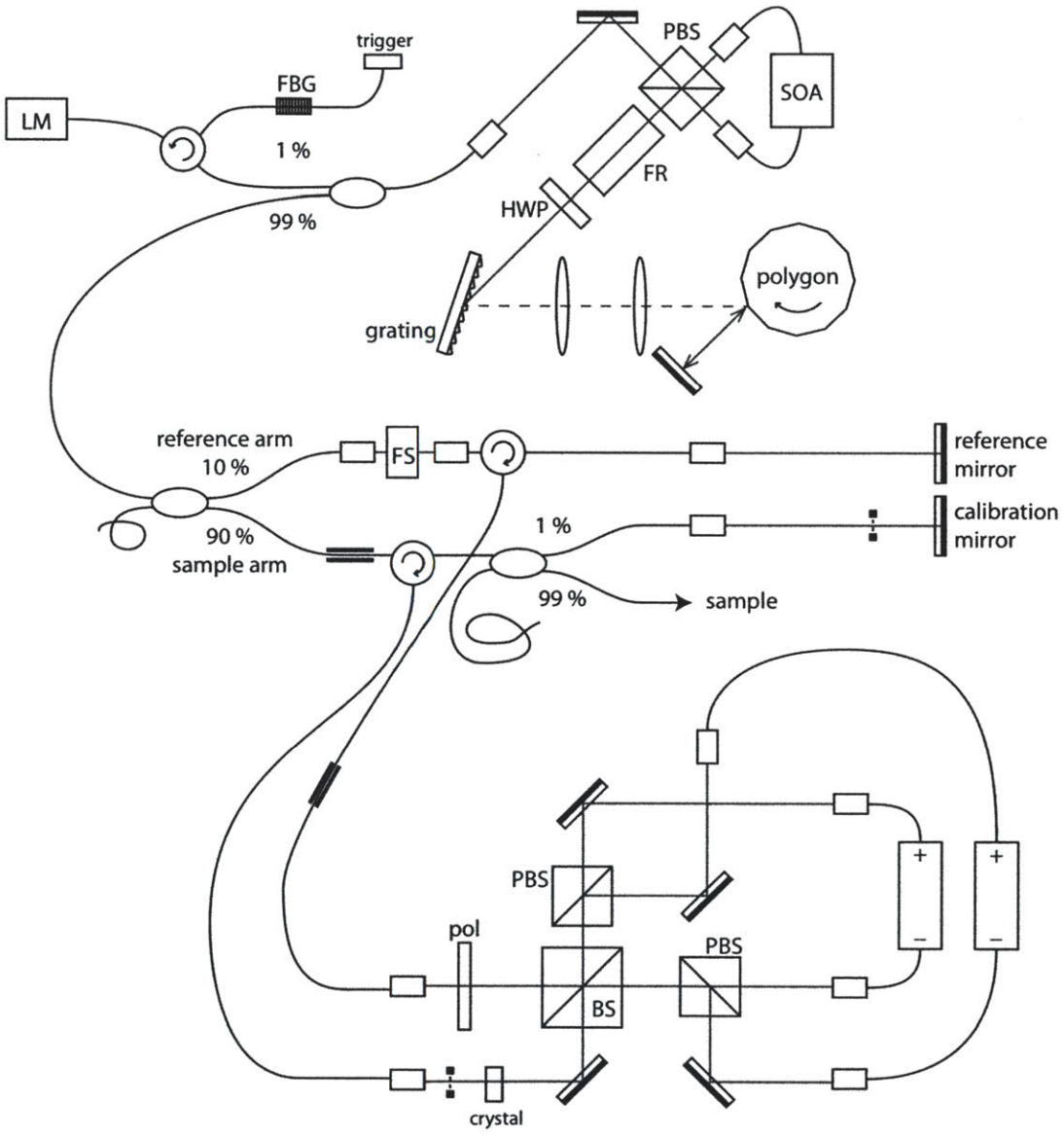

Figure 3-2: Schematic of the optical subsystem.
FBG: Fiber Bragg grating; LM : Laser monitor; FS : Frequency shifter; pol : 45° polarizer

3.1.3 Polarization Sensitive Balanced Receiver

The system employs a polarization sensitive balanced detection, as illustrated in Figure 3-2. The reference arm polarization is controlled to be 45 degrees at the beamsplitter. To compensate for the dispersion caused by the crystal in the optical frequency shifter in the reference arm, the same type of crystal is inserted in the sample arm. A computer-controlled shutter is installed in the sample arm to block the backscattered sample field while only the reference field is recorded to obtain a background signal that is used in the post processing process.

3.1.4 Breadboard Assembly

The breadboard construction of the whole optical subsystem is photographed in Figure 3-3 and Figure 3-5.

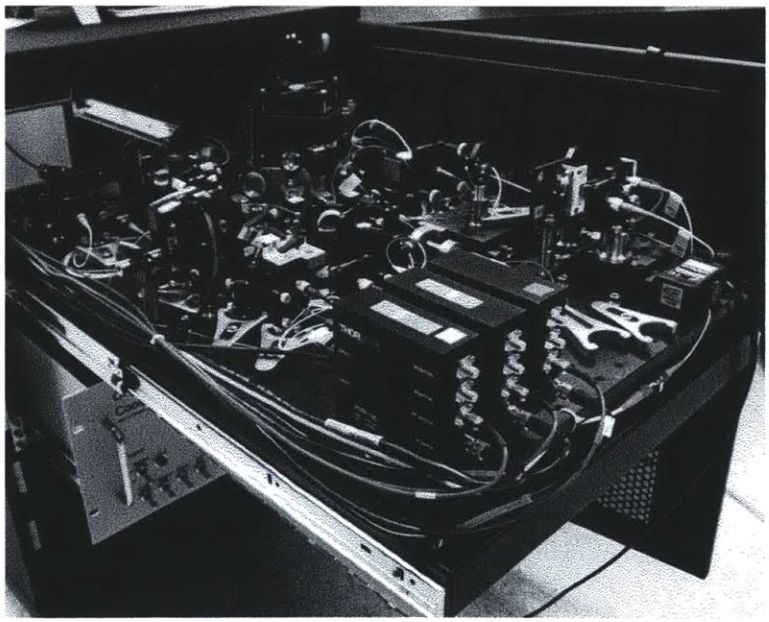

Figure 3-3: Photograph of the optical breadboard on a sliding shelf.

To construct the system in a compact space, aluminum mounts were designed for the beamsplitters, the polygonal mirror, and the SOA. The designed mounts are presented in Figure 3-4. The design considerations include compatibility with

commercial opto-mechanical products; placement of the optical post and the clamping forks of surrounding elements; and flexibility in position adjustment. The drawings for each component are provided in Appendix C.

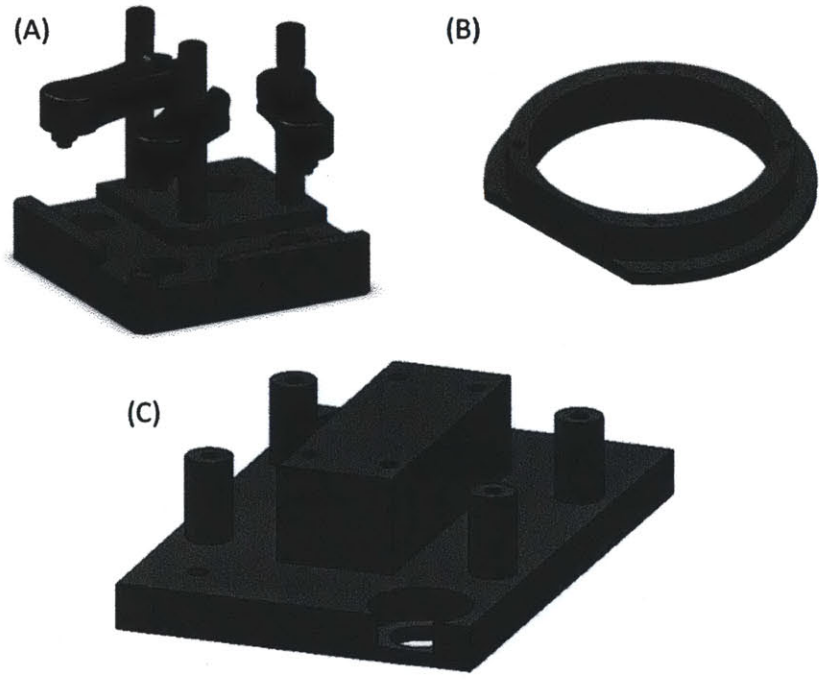

Figure 3-4: The designed mounts for (A) the beamsplitters in receiver, (B) the polygonal scanner and (C) the SOA.

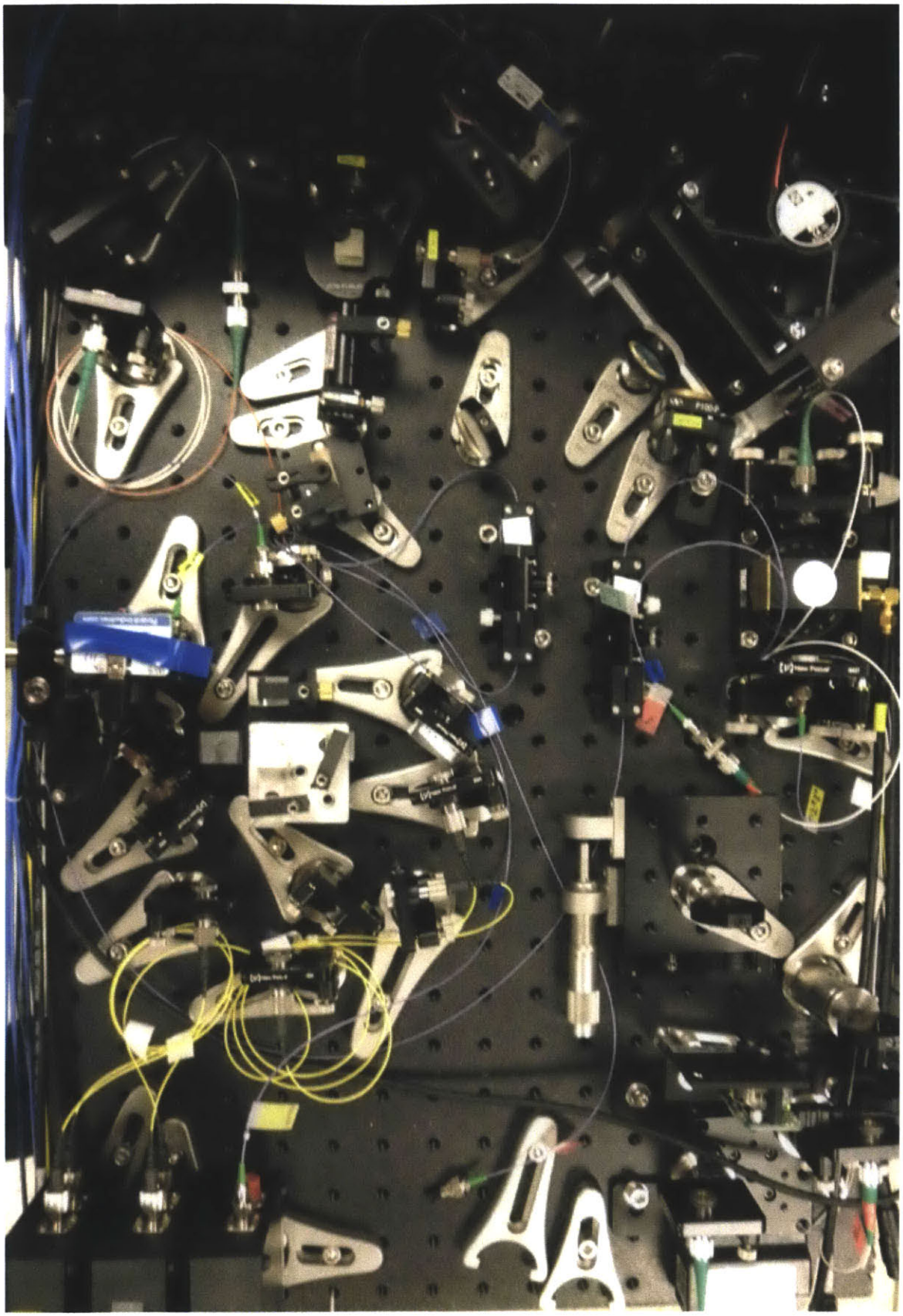

Figure 3-5: Photograph of the optical breadboard in the cart (top view)

3.2 Control Box

The metal case that contains all electronics will be referred to as the control box from this point. The control box is mounted on a sliding guiderail and placed in the portable cart.

3.2.1 Case Design

The case was designed with Protocase Designer 4 software. Figure 3-6 presents the design of the case. The width and the depth were constrained to fit in a standard server rack in the cart, and the height was 4 U (rack server units).

Figure 3-6: Schematic of the empty Control Box.

As seen in Figure 3-7, the front panel of the case includes ventilation holes, power switches, and BNC outputs for monitoring the laser and the galvanometer scanner. The back panel serves as a connection interface where all wires are mounted with a mate-and-lock cable connectors. The construction involved re-assembling of all cables with appropriate connectors. For cables with high currents, we installed mechanical

screw fixers to fix the cables with cable ties on the screws.

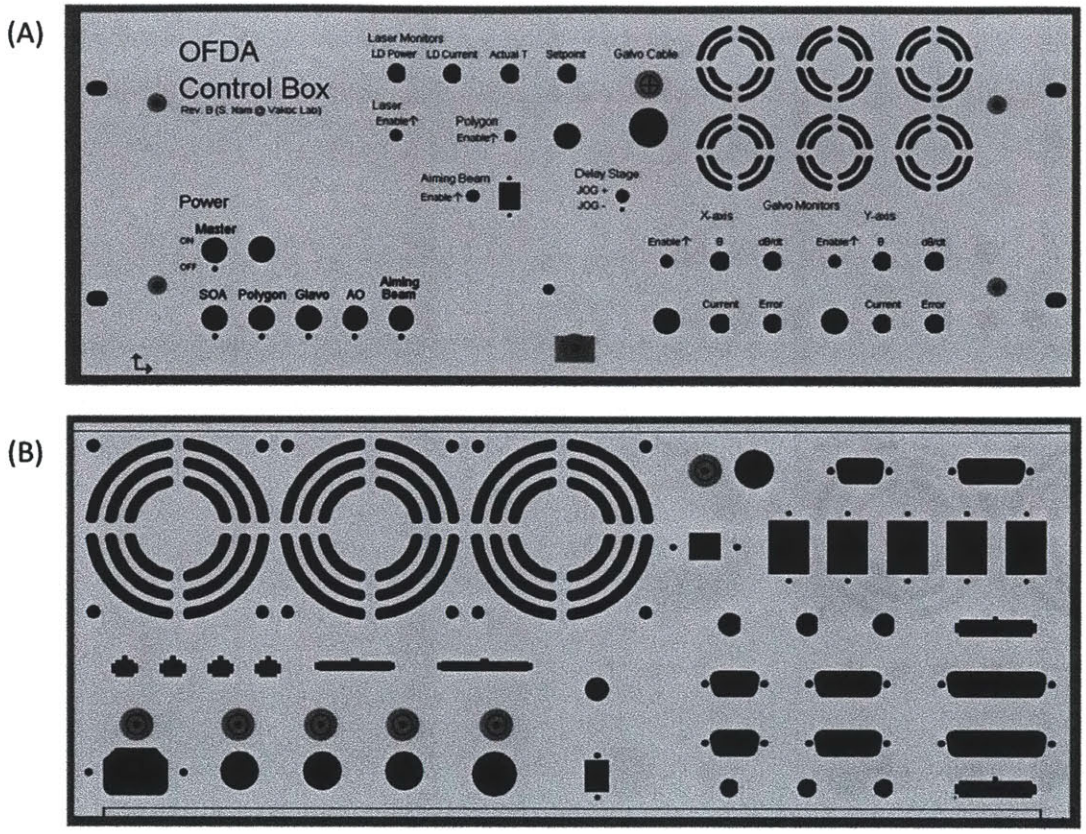

Figure 3-7: The Control Box interface viewed from (A) the front and (B) the back.

3.2.2 Power Connection

The control box encloses all the power supplies of the system components. Each component was matched with an appropriate power supply. The scheme of the power control is illustrated in Figure 3-8. The main switch connects 115 V AC input to the main LED and other first level electronics such as ventilation fans; a temperature monitor; the delay stage with the reference and the calibration mirrors; the balanced detectors in the polarization sensitive receiver part; and the motorized linear stages in the microscope. The power adapters that connect components to AC power are not depicted in the diagram. Secondary switches connect the 115V DV input to the optical frequency shifter, the power supplies of the galvanometer scanner

driver, the polygon driver, and the laser driver. Enable switches are installed for the galvanometer scanner, the polygon scanner, and the SOA.

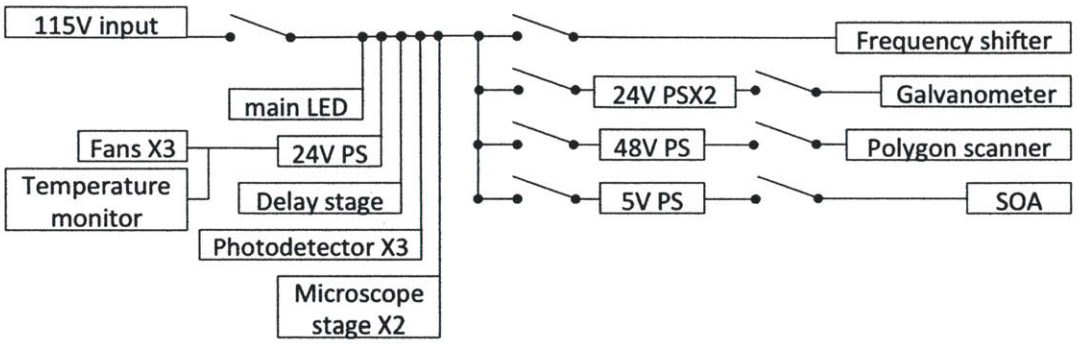

Figure 3-8: Control Box power connection. PS : power supply

3.2.3 Component Layout

One of the challenges in the construction was placing all components in the compact space. To make the best use of the space, some components were stacked on a plate supported by aluminium posts. The bottom of the control box was designed so that the components can be fixed with standard screws or cable ties. Figure 3-9 presents a photograph of the completed control box taken from the top without the top panel.

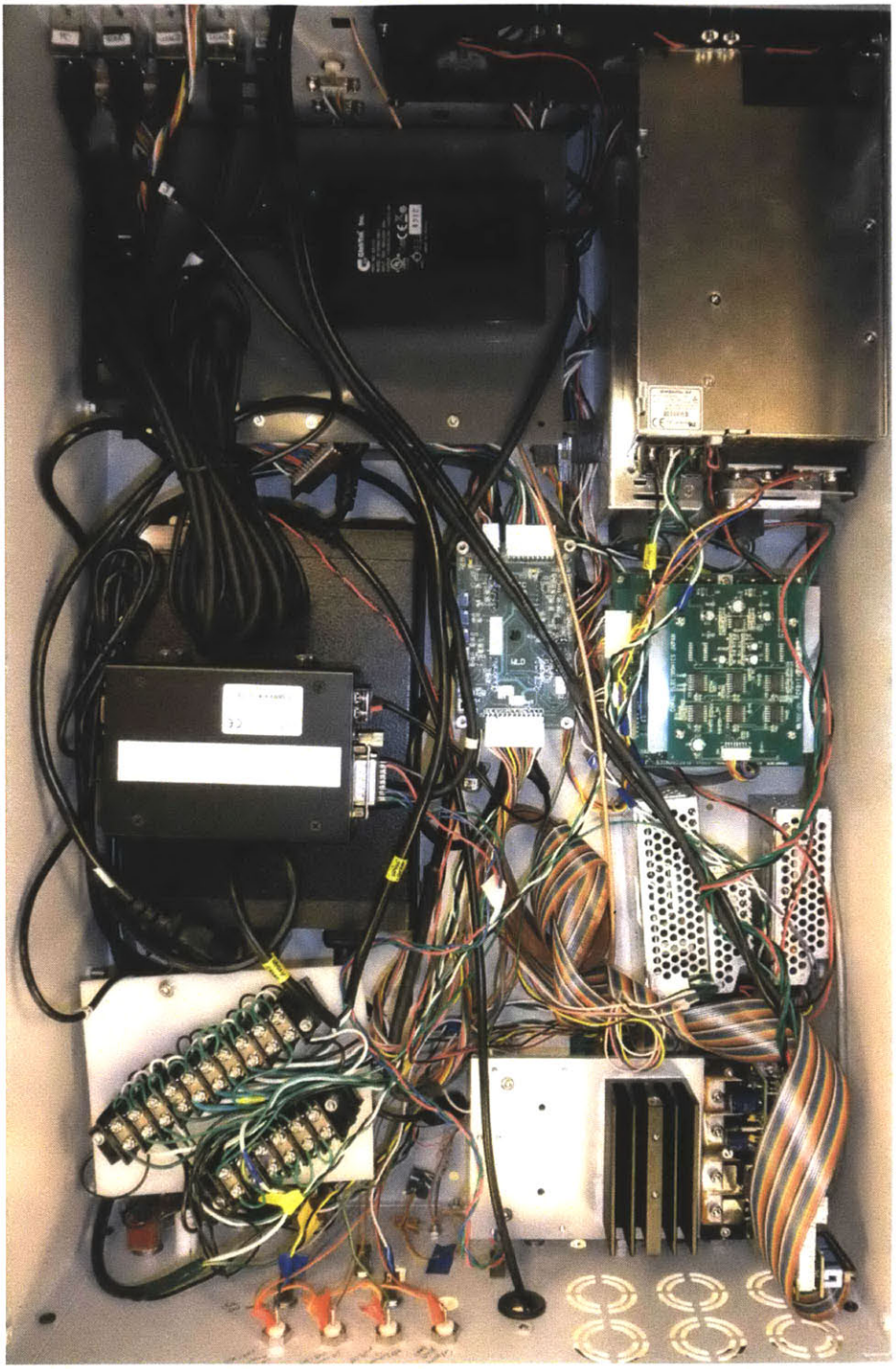

Figure 3-9: Photograph of the control box in the cart (top view)

3.3 Microscope

The microscope provides the interface between the sample and the optical subsystem. The microscope subsystem comprises an objective lens, a two dimensional linear stage, and a galvanometer mirror scanner. The microscope is attached to the cart via an articulating arm so that it can be placed as desired while imaging patients.

3.3.1 Lens selection

IAs mentioned in Section 2.1.1, a good transverse resolution is achieved via a high NA at the expense of large depth of focus. In the ideal case, it is desired to maintain high transverse resolution over the full depth of focus (Figure 3-10). One of the

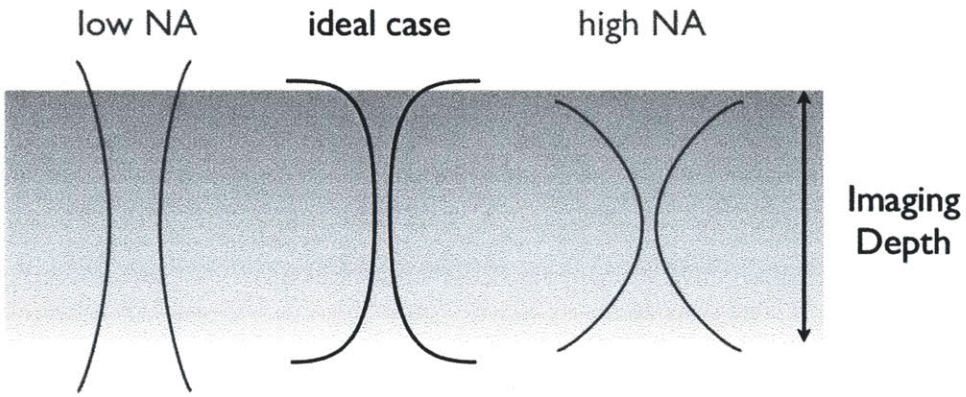

Figure 3-10: The transverse resolution and the depth of focus - coupled with the NA

ideas to address this problem is to image three different depth sections with three separate light sources that are centered at different wavelengths. By taking advantage of chromatic aberration, different sources can be focused at different depth planes, which is illustrated in Figure 3-11.

To select the objective lens that provides sufficient chromatic aberration to focus different source at enough separation distance, beam diameters over the depth have been calculated with ZEMAX software. LSM02 from Thorlabs was chosen, since the total focal shift was 1 mm in free space, which translates to sufficient depth of focus when imaging biological samples. Figure 3-12 plots the root mean square (RMS) beam

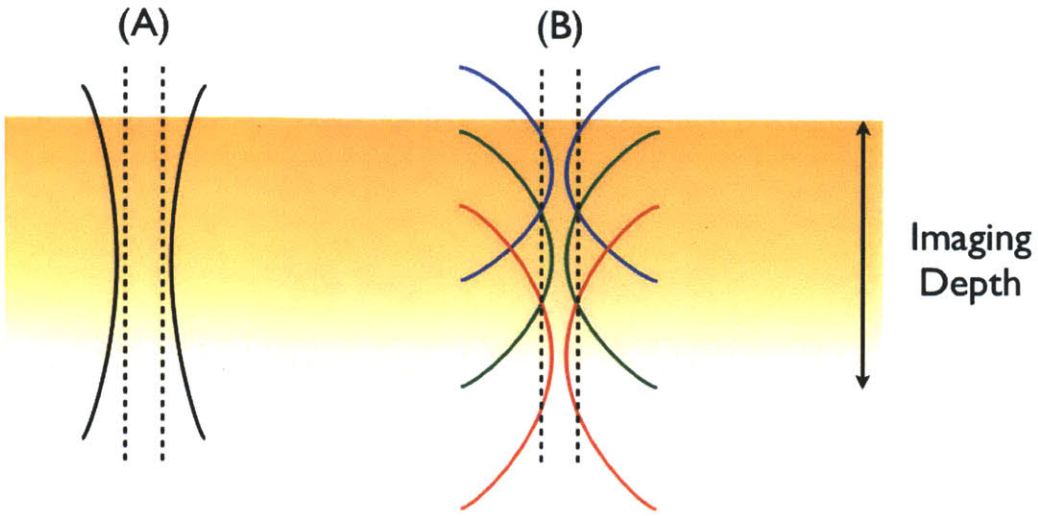

Figure 3-11: Improvement in transverse resolution with tri-band source

spot radius along the depth. The focal shift Δf was calculated from the equation: $\Delta f = z0 - z$, where z_0 is the back focal length from the lens surface at the wavelength 1300 nm.

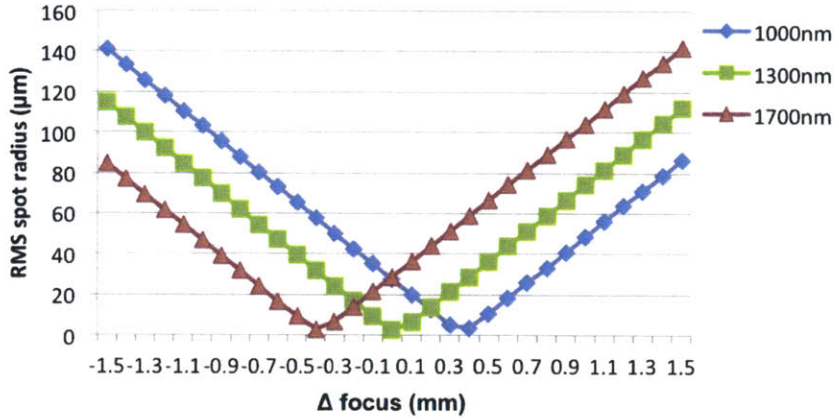

Figure 3-12: RMS Spot radius.

3.3.2 Transverse Scanning

We have implemented an one-dimensional galvanometer scanner to achieve a tomographic cross-sectional image, and a bi-directional motorized linear stage to move the lens with respect to the sample to obtain volume information as well as to adjust the

lens position. The scan priority is diagrammed in Figure 3-13

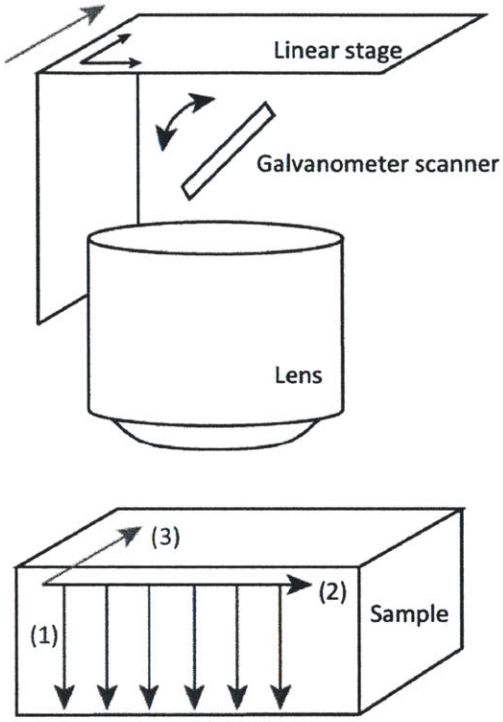

Figure 3-13: Schematic of the scanning mechanism. red : z-direction depth scan provided by the laser sweep; blue : x-direction transverse scan provided by the galvanometer; green : y-direction transverse scan provided by the linear stage.

3.3.3 Objective Interface Design

The objective interface is designed to image the dermal microvasculature of human patients. To facilitate the process, a commercial adhesive window for dermal confocal imaging is employed. The window is designed to interface a magnetic ring and the imaging site. The magnetic ring attaches to an adapter piece, which can be adjusted to find the best focus. The magnet mechanism enables simple attachment and detachment with an outer ring. The basic concept is diagramed in Figure 3-14, and a photograph of the microscope is shown in Figure 3-15.

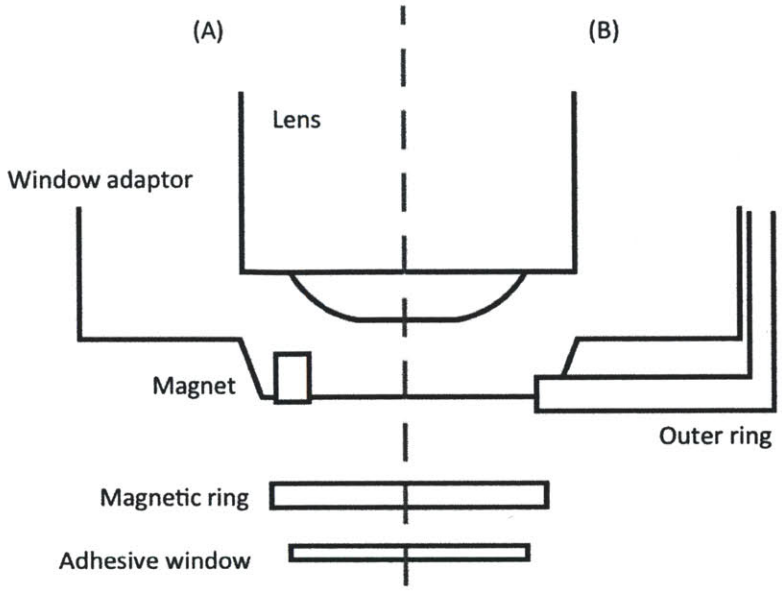

Figure 3-14: Schematic of the skin-objective interface (A) without the outer ring and (B) with the outer ring.

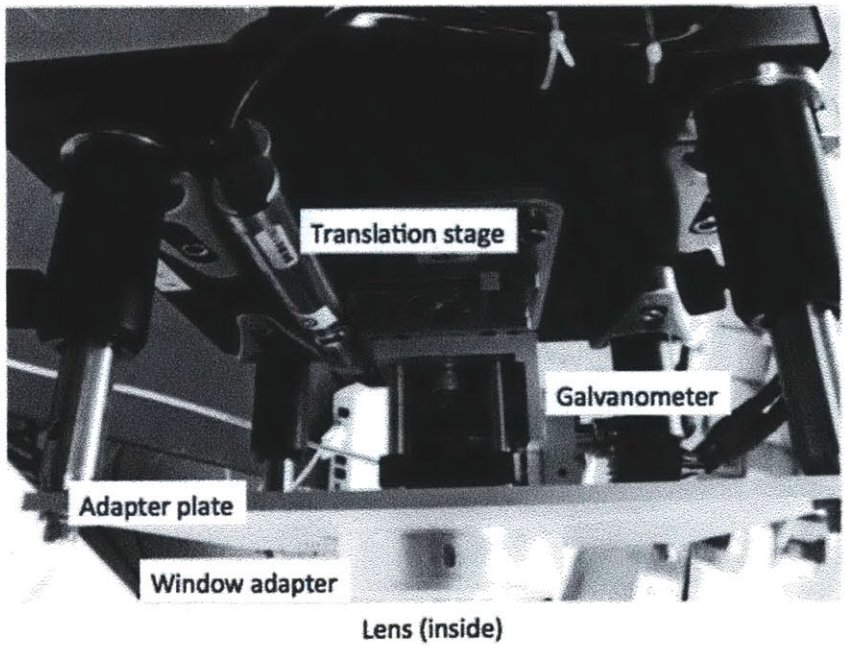

Figure 3-15: A photograph or the microscope.

3.4 Construction

The whole system is encased in a portable cart (61 cm×101.4 cm×92.9 cm, W×D×H) with a monitor and the microscope attached to it. A computer (Windows 7, a 2.67 MHz quad core CPU, a 12 GB RAM) of a height of 1 U (rack server unit) is inserted at the top. The optical breadboard where all optical elements are fixed with clamping forks is mounted on a sliding server rack self. A thin aluminum panel was attached under the sliding shelf. On the panel, fiber based elements such as couplers and circulators were laid out. The control box is mounted on a set of guide rail and installed under the optical breadboard. At the bottom of the cart, an electrical power isolator is installed.

The microscope is mounted on an articulating arm (42 inches maximum length). The double arm is gas spring assisted so it can be effortlessly pulled and positioned as desired. It provides up to 42" of vertical and horizontal adjustment with 180 degrees rotation. The head part is ball-jointed to allow the fine-tuning of the position. The arm is fixed on the left panel of the cart. Cables that connects controllers in the controller box to the galvanometer and the linear stage are fixed tight with tie straps so the connections are robust. The Optical fiber in the sample arm is protected in a 3 mm diameter outer jacket and also tied securely to the microscope with tie straps.

Figure 3-16 shows a schematic of the complete system on the cart. A complete list of parts is included in Appendix C and a list of connectors and electronic cable components is included in Appendix D.

3.4.1 Challenges

The main challenge of this work was building the system from scratch. Component purchases involved comparing similar products from different manufacturers and selecting the ones that meet desired specifications. Simulation and design required softwares (Zemax and Solidworks) that I have never been exposed to before. Basic resources such as screws and bolts also had to be purchased as well as electrical cable connectors and wire crimps.

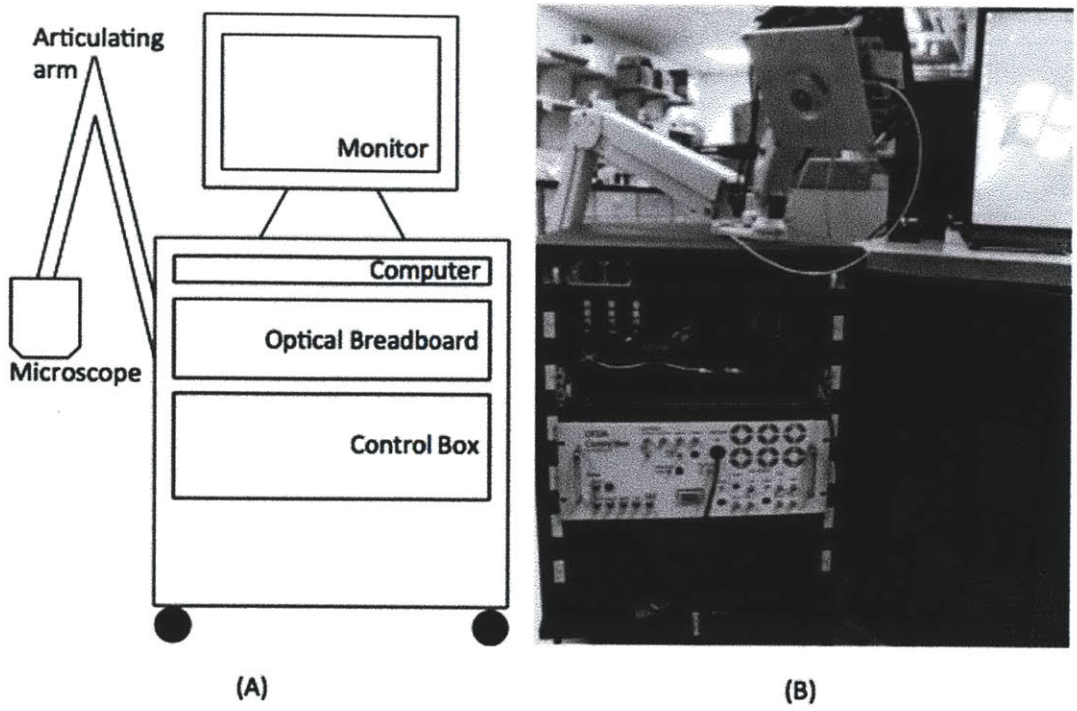

Figure 3-16: System. (A) A Schematic and (B) a photograph.

Like other experimental studies, this project required solid understanding of the theory as well as experience and insight in laboratory. As I did not have a background in Optics, understanding the physics of OCT and OFDI was challenging in the beginning. In the laboratory, aligning all free-space optical components to minimize power loss have been quite tedious.

Planning had gone through a great amount of trial-and-error, specifically for the planning the work in between the purchase and the delivery of a component. Devices occasionally broke down, identifying the cause and repairing them also took some unexpected time.

Chapter 4

Performance and Future Work

This chapter presents the performance of the system. The image obtained from the system is what we believe to be the first image of human dermal vasculature imaged without any exogenous agents. The system will be further improved and applied for clinical studies in dermatology in the future.

4.1 Laser Performance

The performance of the system is largely determined by the source characteristics, since the balanced receiver and DAQ are commercial products and the image-processing algorithm is already optimized for vasculature OFDI.

4.1.1 Coherence Length

The coherence length was measured by finding the calibration mirror delay that causes the fringe amplitude to decrease to the half of the path-match fringe amplitude. The path-match was found with an RF spectrum analyzer when the peak occurred at a 40 MHz signal frequency. The coherence length was measured to be 3.15 mm to the positive side of the spectrum and 3.30 mm to the negative side of the spectrum, which satisfies the goal described in Chapter 3.1. Figure 4-1 shows the oscilloscope signals at the pathmatch and at the maximum ranging depths.

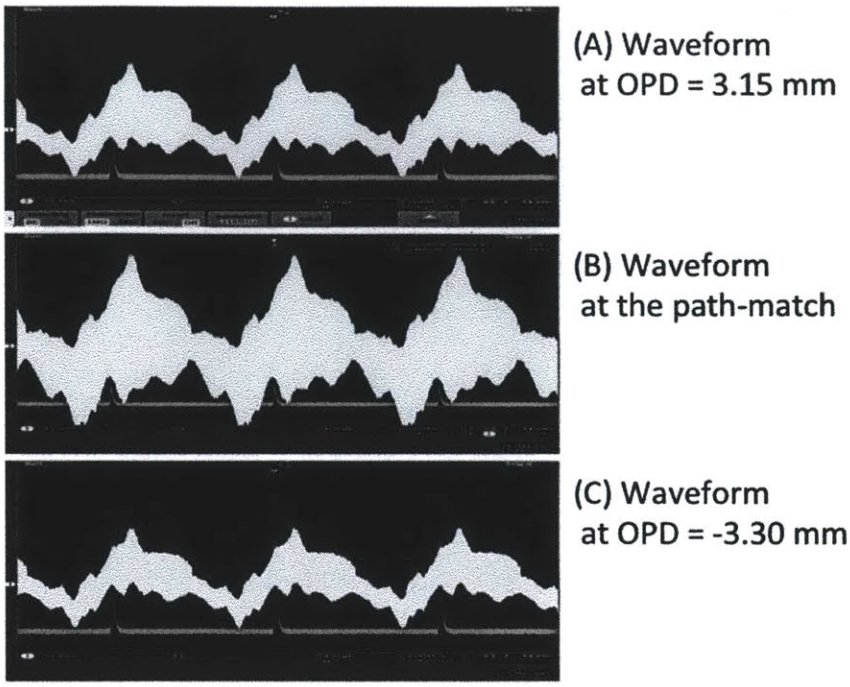

Figure 4-1: The oscilloscope signals.

4.1.2 Source Spectrum

As described in Section 2.2.1, the source spectrum determines the axial resolution of OFDI. The source had a bandwidth of 140 nm, as measured by an optical spectrum analyzer (OSA).

4.2 Image and Discussion

The vasculature of human cheek skin is imaged for testing purposes. The adhesive window with index-matching gel was placed on the cheek of a subject while the person was sitting on a chair. The field of view was set at 7.2 mm $\times$ 5.6 mm. Data acquisition time was 54 seconds. Figure 4-2 displays an *en face* image of human cheek vasculature. The vessels are color-mapped along the depth into the skin: yellow (superficial) to red (deep).

We believe optimization of the processing algorithm and scan pattern will provide more contrast. In addition, employing thicker objective window with anti-reflective

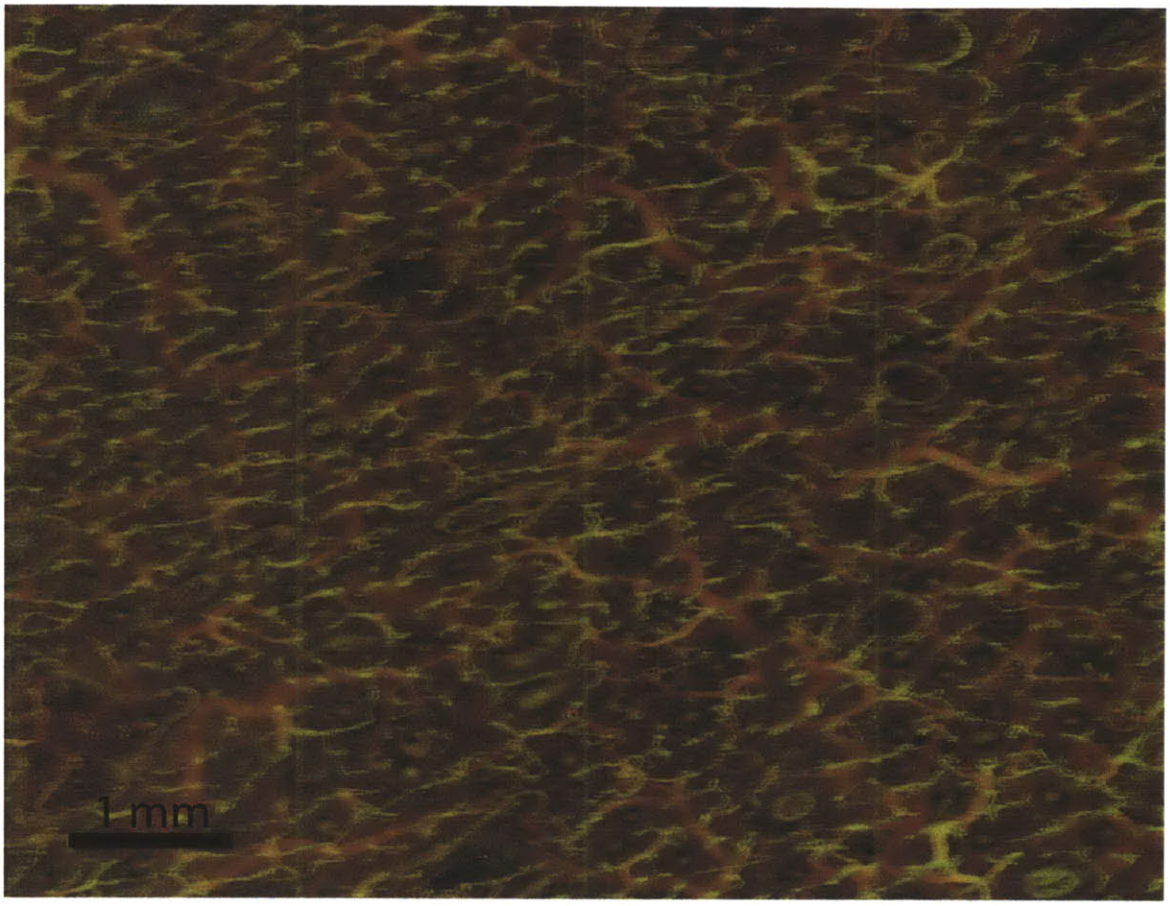

Figure 4-2: *In-vivo* image of the human cheek vasculature.

coating will also remove the undesired vertical striation.

4.3 Future Work

Plans for further research can be summarized as (1) application of the system for the study of port wine stain (PWS) treatment and (2) optimization of optical system performance.

After the system is validated, we will investigate the kinetics of microvascular response of PWS to the pulsed-dye laser (PDL) therapy. We will be working with dermatologists in Massachusetts General Hospital and Brigham and Women Hospital. We will recruit and obtain consent from a group of adult volunteers seeking treatment for PWS. The patients will be treated up to 8 times, and image of capillary structure in

lesion will be taken prior and immediately after the treatments, and also at follow-up appointments. This study aims to provide guidelines for the most effective parameters for the therapy through understanding of the biology at microvascular level.

While the current system presents valuable and promising imaging of capillary structure, its performance can still be improved. To better discriminate capillaries in skin, a uniform transverse resolution throughout the depth is advantageous. In the current OFDI system, high transverse resolution is limited to 25-30m for a 1mm depth of field. Higher resolution is usually achieved at the expense of penetration depth. I have planned to develop a laser source that can penetrate deeper (2mm) in the skin with better resolution (~10m). The concept has been validated through simulation results. As discussed in Section 3.3.1, the lens was chosen so that it provides sufficient focal shifts between three different bands of wavelengths (1000 nm, 1300 nm, and 1700 nm).

The shorter and longer regime sources will be incorporated into the current system. Since different wavelengths focus at different depths with longer wavelength at a deeper position, three separate band of signal is obtained. These data can be merged in to one image at the processing step.

Appendix A

Short Cavity WSL Alignment

1. Collimation adjustment (with a collimator to mirror distance of 25 cm)

   (a) Adjust collimator(3) first.

   (b) Collmator(1) and (2) are connected to the PM fiber which has a different NA to SMF, so they can not be collimated by monitoring the coupled power. Adjust collimation by observing the beam size so that it is maintained constant over the distance.

2. Height Matching

   (a) All heights should match the opening of the polygon mirror.

   (b) Adjust collimators first, and also adjust the PBS mount so that the beam does not bend up or down after the PBS. Also adjust the vertical angle of the grating.

3. Layout and polarization adjustment

   (a) Mount the SOA so that its arrow points toward the direction of collimator(1).

   (b) Adjust the mounting angle of collimator(1) to have 50/50 split after the PBS.

(c) Adjust the mounting angle of collimator(2) to have maximum light going into the telescope.

4. Output coupling

   (a) Maximize the coupling between the collimator(1) and (3) by adjusting the knobs on the output mirror and collimator(3).

5. Source alignment

   (a) Place a temporary mirror in place of the grating, and align to gain lasing power of 50mW at least in the free space before the collimator(3). Adjust the knobs on the temporary mirror first and then the ones on the collimator(2).

6. Telescope alignment

   (a) The half wave plate can be either at 22.5 or 67.5. Choose the angle that makes the 0th order diffraction power of the grating the minimum.

Appendix B

Frequency Shifter Alignment

1. Match heights of the collimators and the AO holes.

2. Obtain a good 0th order coupling with the AO off. With the AO off, diffraction does not occur so the beam must be in a regular circular shape. If it is chipped, this indicates that it does not go through the crystal properly.

3. Turn the AO on. Twig the rotation mount slightly to make one of the first order beam is the brightest. Place the IR card long enough away from the beam so there is clear separation. Taking out the receiving collimator may help. Check whether it is the first order by switching the AO on and off. With the AO off, only the 0th order exists.

4. Put the receiving collimator back in, and turn the AO off. Align again for a good 0th order coupling. Do not touch the first collimator or the AO. Only adjust the second collimator. (This coupling need not be as good as the coupling at Step 2.)

5. Turn the AO on, adjust lateral angle of the second collimator to find the 1st order spot. Try to remember where the bright 1st order was and turn to that direction. This turn may be quite far. Note that 1st order power can be very small.

6. Slowly optimize this 1st order coupling, by adjusting the collimators, then adjusting the AO. Care must be taken not to lose the 1st order coupling.

Appendix C

Components List

Part	Components	Vendor	Model Number	Description	Quantity
Housing	rack-case	supermicro			
Housing	custom control box	protocase			
Housing	sliding guide rail	McMaster-Carr	2005A7	for the control box ;Narrow Lock-Open Side-Mount STL Drawer Slide Full Extension, 24" L, 26" L Travel, 110 lb/Pr	1
Housing	sliding shelf	Digi-Key	RSVS1926BK1-ND	SHELF SLIDE 26.1X16.6X1.5" BLACK Hammond Manufacturing (#:RSVS1926BK1)	1
Housing	sponge	McMaster-Carr			1
Housing	arm	ICW USA			
Housing	cardboard	bellcomb	8458K14	Improved-Strength Basic Aluminum Honeycomb Panel, 1/8" Thick, 24" X 24"	1
Bread Board	breadboard	Thorlabs	MB1824	Aluminum Breadboard, 18" x 24" x 1/2", 1/4"-20 Threaded	1
aiming beam	laser	Blue Sky Research	FMXL532-005-SAOB	532 nm fiber coupled laser, 5 mW	1
aiming beam	driver	Wavelength Electronics	LDD400	laser diode current supply	1
aiming beam	driver board	Wavelength Electronics	LDDEVALP	evaluation board	1
aiming beam		Wavelength Electronics	WCB201	cable	1

Part	Components	Vendor	Model Number	Description	Quantity
Laser	Rotation mount	Thorlabs	PRM05	High Precision Rotation Mount for Ø1/2" (12.5 mm) Optics	1
Laser	Half wave plate	Newport	05RP02-37	Zero-Order Quartz Wave Plate, 12.7mm Dia, 1315nm, λ/2 Retardation	1
Laser	Faraday Rotator	Isowave	I-13-FR-4	Faraday rotator	
Laser	Grating	Edmund Optics	NT46-080	830 Grooves, 1200nm NIR Ruled Grating, 25mm Square	1
Laser	Lens1	Edmund Optics	NT45-804	NIR Achromatic Lens 25mm Dia. x 60mm FL, NIR-II Coating	1
Laser	Lens2	Edmund Optics	NT45-801	NIR Achromatic Lens 25mm Dia. x 40mm FL, NIR-II Coating	1
Laser	PBS	Newport	05FC16PB.9	PBS Cube 12.7 mmBroadband Polarizing Cube Beamsplitter, 12.7 x 12.7 x 12.7 mm, 1200-1600 nm	1
Laser	PBS mount	Newport	9481	Pint-Sized Prism Mount, 0.25 to 1.00 in., ±3.5 °, 8-32	1
Laser	End mirror mount	Newport	P100-P	Platform Optical Mount, 1.0 in. Diameter, ±6° Knob Adjustment, 8-32 Thread	2
Laser	Coll/Mirr mount	Newport	9884	Pint-Sized Corner Mirror Mount, 1.0 in. Diameter, 3 Knob Adjustment	3
Laser	Pedestal posts (3/8	Newport	9943	0.7 in. Optical Pedestal, 0.5 in. Height, 8-32 Thread	8
Laser	Pedestal posts (1"H	Newport	9944	0.7 in. Optical Pedestal, 1.0 in. Height, 8-32 Thread	3
Laser	Clamping forks	Newport	9947	Clamping Fork, Small Pedistal, Captive 1/4-20 Screw	11
Laser	Pedestal spacers (1	Newport	SP-0.25-S-10	Mini Pedestal Spacers, 1/4 in. Thick, 0.5 in. Diameter, 8-32 (M4) CLR, Bag of 10	1
Laser	Pedestal spacers (1	Newport	SP-0.125-S-10	0.5 in. Optical Pedestal Spacers, 1/8 in. Thick, 8-32 (M4) CLR,Bag of 10	1
Laser	Mirror	Edmund Optics	NT-45-606	1/4λ Mirror 25mm Diameter Protected Gold	2
Laser	grating clamping arm	Thorlabs	PM1	Small Clamping arm	3
Laser	Grating stage	Optosigma	123-2210	Tilt Platforms / Tilt Stage 2 Axis /	1
Laser	Collimator	Thorlabs	CFC-8X-C	Adjustable Aspheric Collimators (f=7.5 mm, NA = 0.30)	3
Laser	Collimator Adapter	Thorlabs	AD9.5F	SM1 Adapter for Ø9.5 mm Collimators	3
Laser	Lens mounts	Thorlabs	FMP1	Fixed Ø1" Optical Mount	2
Laser	polygon mount clamp	thorlabs	CL5	General Purpose Clamp	2
Laser	SOA	Thorlabs	BOA1130P	O-Band Booster Optical Amplifier, CWL=1285 nm, Butterfly Pkg, PMF, FC/APC	1
Laser	laser driver power supply	TDK-Lambda	HK25A-5/A	single output 25W	1
Laser	laser driver/temp controller	Wavelength Electronics	LDTC 2-2 O	Laser Driver & Temp Controller	1
Laser	polygon	Copal			1
Laser	polygon mount	FirstCut	designed		1
Laser	SOA holding clips	Azimuth electronics		left / right set	1
Laser	SOA mount			designed	1
Laser	50/50 coupler	Gould Fiber Optics	45-10331-50-22261	50/50 fused coupler	1
Laser	1/99 coupler	General Photonics	45-10331-01-22261	99/1 fused coupler	1
Laser	Monitor detector	Thorlabs	DET01CFC	FC Input Biased InGaAs Photodetector	1

Part	Components	Vendor	Model Number	Description	Quantity
aiming beam	laser	Blue Sky Research	FMXL532-005-SAOB	532 nm fiber coupled laser, 5 mW	1
aiming beam	driver	Wavelength Electronics	LDD400	laser diode current supply	1
aiming beam	driver board	Wavelength Electronics	LDDEVALP	evaluation board	1
aiming beam		Wavelength Electronics	WCB201	cable	1
interferometer	AO freq shifter	Brimrose	AMF-40-1300	free space 40MHz frequency shifter	1
interferometer	PC	General Photonics	PLC-003-S-90	polarization controller	2
interferometer	90/10 coupler	Gould Fiber Optic	45-10331-10-22261	90/10 fused coupler	1
interferometer	99/1 coupler	Gould Fiber Optic	45-10331-01-22261	99/1 fused coupler	1
interferometer	Circulator	Gould Fiber Optics	CIRC-3-31-P-BB-15-C	Circulator, 3 port, 1310nm, Premium grade,900um loose tube package, 1.5 meter lead,FC/APC connectors	2
interferometer	clamping fork	New Focus	9916	Clamping Fork, Short	2
interferometer	pedestal riser (0.5H)	New Focus	9951	Fixed Stainless Steel Pedestal, 0.5 in Height, 1.0 in. Diameter, 8-32 Thread	2
interferometer	kinematic 1" mount	New Focus	9807	Classic Center Mirror Mount, 1.0 in. Diameter, 3 Knob Adjustment	2
interferometer	Post hight washers set	New Focus	9950	Pedestal Shim Set, Includes (3) 0.25 in. and (6) 0.125 in. Shims	1
interferometer	FBG	O/E Land	13-025-3-7191	fiber bragg grating	1
interferometer	Collimator (5X)	Thorlabs	CFC-5X-C	Adj. FC/PC and FC/APC Collimator, f = 4.6 mm, ARC: 1050-1620 nm	2
interferometer	Collimator adapter	Thorlabs	AD9.5F	SM1 Adapter for Ø9.5 mm Collimators	2
interferometer	Rotation platform	Thorlabs	RP01	Rotation Platform	1
interferometer	Thread adapter	Thorlabs	AP8E4E	Thread Adapter, External to External, #8-32 to #4-40	1
interferometer	Thread adapter	Thorlabs	AP8E25E	Thread Adapter, External to External, #8-32 to 1/4-20	1
Reference stage	Mirror	Edmund Optics	NT45-606	1/4λ Mirror 25mm Diameter Protected Gold	2
Reference stage	clamping fork	New Focus	9916	Clamping Fork, Short	4
Reference stage	mini 1" mounts	New Focus	9884	pint-sized 1" corner mount	2
Reference stage	mini transl stg	New Focus	9065-x	pint-sized x-translation stage : Triple Divide X Axis Translation Stage, 0.55 in. Travel, 8-32, 1/4-20	1
Reference stage	mirror mount	Thorlabs	FMP1	Fixed Ø1" Optical Mount	2
Reference stage	pedestal riser (0.75H)	New Focus	9957	Fixed Stainless Steel Pedestal, 0.75 in Height, 1.0 in. Diameter, 8-32 Thread	1
Reference stage	post (2"H)	New Focus	9954	Fixed Stainless Steel Pedestal, 2.0 in Height, 1.0 in. Diameter, 8-32 Thread	3
Reference stage	screw set	New Focus	9368	Braked screw set; 0.75" travel; 100 TPI	1
Reference stage	slim post (1.5"H)	Newport	SP-1.5	Standard Post, 0.5 in. Diameter x 1.5 in., 8-32 & 1/4-20 Tapped Holes	2
Reference stage	delay stage	Optosigma	511-2011 (SGSP20-20 (X)-INCH	motorized translation stage; SGSP20-20SGSP Linear Stages / Linear Stepping Motor Stage / 511-2011-INCH	1
Reference stage	delay stage	Optosigma	555-5030	stage controller; PAT-001	1

Part	Components	Vendor	Model Number	Description	Quantity
Reference stage	delay stage	Optosigma	555-5035	Power adapter for PAT-001-POW	1
Reference stage	delay stage	Optosigma	541-4050	stage adapter plate	2
Reference stage	delay stage	Optosigma	561-1022	Mini type cable, L=2m #MINI-CA-2	1
Reference stage	delay stage	Optosigma	561-2531	RS232C interface cable; 1.8m	1
Reference stage	shutter	Picard Industries	USB-SHUT	USB controlled shutter	1
Reference stage	Collimator adapter	Thorlabs	AD9.5F	SM1 Adapter for Ø9.5 mm Collimators	2
Reference stage	Collimator	Thorlabs	CFC-8X-C	Adjustable Aspheric Collimators (f=7.5 mm, NA = 0.30)	2
Reference stage	BS cube	Edmund Optics	NT47-235	BS cube	1
Reference stage	post holder	Newport	VPH-2-P	Standard Pedestal Post Holder, 2.19 in., For Post Dia. 0.5 in.	1
Receiver	freq shifter crystal	Brimrose	N/A	Amtir Crystal Cube	1
Receiver	BS cube	Edmund Optics	NT47-235	BS cube	1
Receiver	mirrors	Edmund Optics	NT45-606	1/4λ Mirror 25mm Diameter Protected Gold	4
Receiver	thick mirrors	Edmund Optics	NT43-408-566	1/20Wave Flat Fused Silica 1" Dia. Gold	1
Receiver	BS mount	FirstCut	designed		1
Receiver	clamping fork	New Focus	9916	Clamping Fork, Short	10
Receiver	mini 1" mounts	New Focus	9884	pint-sized 1" corner mount	10
Receiver	pedestal riser (0.5"H)	New Focus	9951	Fixed Stainless Steel Pedestal, 0.5 in Height, 1.0 in. Diameter, 8-32 Thread	10
Receiver	right angle clamp	New Focus	9935	Right angle post clamp	1
Receiver	slim post (1"H)	Newport	SP-1	Standard Post, 0.5 in. Diameter x 1 in., 8-32 & 1/4-20 Tapped Holes	3
Receiver	PBS	Newport	05FC16PB.9	PBS Cube 12.7 mmBroadband Polarizing Cube Beamsplitter, 12.7 x 12.7 x 12.7 mm, 1200-1600 nm	3
Receiver	shutter	Picard Industries	USB-SHUT	USB controlled shutter	1
Receiver	Collimator adapter	Thorlabs	AD9.5F	SM1 Adapter for Ø9.5 mm Collimators	6
Receiver	Collimator	Thorlabs	CFC-8X-C	Adjustable Aspheric Collimators (f=7.5 mm, NA = 0.30)	6
Receiver	MMF jumpers	Thorlabs	special order placed	L=0.5,FC,PC,FT900SM ; Fiber:GIF50, Protective tubing FT900SM, connector end1: FC/PC end2: FC/PC	4
Receiver	pol cube mount	Thorlabs	VC1	small v-clamp	2
Receiver	BS clamping arm	Thorlabs	PM1	small clamping arm	2
Receiver	slim post (2"H)	Newport	SP-2	Standard Post, 0.5 in. Diameter x 2 in., 8-32 & 1/4-20 Tapped Holes	1
Receiver	slim post (1.5"H)	Newport	SP-1.5	Standard Post, 0.5 in. Diameter x 1.5 in., 8-32 & 1/4-20 Tapped Holes	2
Receiver					
Receiver					
Receiver	clamping fork	New Focus	9909	Clamping Fork, Regular	2
Receiver	pedestal riser (0.5H)	New Focus	9951	Fixed Stainless Steel Pedestal, 0.5 in Height, 1.0 in. Diameter, 8-32 Thread	2
Receiver	detector	Thorlabs	PDB110C	balanced photodetect InGaAs, 100MHz, 110V	2

Part	Components	Vendor	Model Number	Description	Quantity
Galvo	USB digital module	Accesio	USB-DO16A-OEM	USB Digital Waveform Generator Module	1
Galvo	Interface board components	Mouser Electronics	653-XG4C-3031	Omron - Headers & Wire Housings Plug Straight Box Type 30 Pins	3
Galvo	Interface board components	Mouser Electronics	617-60-06-068-5440	HARTING - I/O Connectors 68P MALE IDC CABLEMT	3
Galvo	Interface board components	Mouser Electronics	523-132225	Amphenol - RF Connectors SMA R/A JACK PCB DIECAST	2
Galvo	Interface board components	Mouser Electronics	571-3-111196-4	Tyco Electronics - FFC / FPC Connectors 050X100 REC 2X34P	3
Galvo	Interface board components	Mouser Electronics	571-6-104068-8	Tyco Electronics - Board to Board / Mezzanine Connectors 68 POS HDR VERT DUAL ROW	2
Galvo	Interface board components	Mouser Electronics	571-6404558	Tyco Electronics - Headers & Wire Housings POLARIZED HEADER 8P Right Angle Post tin	3
Galvo	Interface board components	Mouser Electronics	571-3-644540-8	Tyco Electronics - Headers & Wire Housings FEED THRU W/TAB 8P red tin 22 AWG	3
Galvo	galvo	Cambridge Technology	6215HM60B	Model 6215HM60B Galvanometer Scanner, AMP connector, +/- 15 MEchanical degrees, +/- 30 optical degrees, slotted shaft	1
Galvo	galvo	Cambridge Technology	671215H-1HP	MicroMax series 6711XX single axis class 1 integrating with the high power option servo driver amplifier for the model 6215H galvanometer. Power supply voltages +/- 24 V to +/- 28V, "A" connector. Sonfigured for 3mm inertia	1
Galvo	galvo	Cambridge Technology	6757	Digital Input Module, 16 BIT, For the MicoMax Model 670XX and 671XX. Includes Interconnect Cable 6013-1-120 with Mating Connector to the 6757 Input	1
Galvo	galvo	Cambridge Technology	6010-36-154LN	Interconnect Cable, 154" low noise	1
Galvo	galvo	Cambridge Technology	6M2003X-S	3mm Mirror	1
Microscope	Breadboard	Thorlabs	MB8	Aluminum Breadboard, 8" x 8" x 1/2", 1/4"-20 Threaded	1
Microscope	Bracket	Thorlabs	AP90RL/M	Large Angle Bracket - Metric	1
Microscope	Post Holders (2"H)	Thorlabs	TR2	Ø1/2" x 2" Stainless Steel Optical Post, 8-32 Stud, 1/4"-20 Tapped Hole	4
Microscope	1/2" posts (2"H)	Thorlabs	PH2E	Pedestal Post Holder, Spring-Loaded Hex Locking Thumbscrew, L = 2.19"	4
Microscope	Clamping forks	New Focus	9916	Clamping Fork, Short	4
Microscope	lens mount rod	Thorlabs	ER1.5	Cage Assembly Rod, 1.5" Long, Ø6 mm	4
Microscope	coll. mount rod	Thorlabs	ER05	Cage Assembly Rod, 1/2" Long, Ø6 mm	4
Microscope	cage plate mount	Thorlabs	CP02	SM1 Threaded 30 mm Cage Plate, 0.35" Thick	2
Microscope					
Microscope	collimator	Thorlabs	CFC-8X-C	Adjustable Aspheric Collimators (f=7.5 mm, NA = 0.30)	1
Microscope	coll. adapter	Thorlabs	AD9.5F	SM1 Adapter for Ø9.5 mm Collimators	1

Part	Components	Vendor	Model Number	Description	Quantity
Microscope	lens	Thorlabs	LSM02	10X OCT Scan Lens, EFL=18 mm, Design Wavelength=1315±65 nm	1
Microscope	set screw	McMaster Carr		#4-40 nylon tip setscrew	1
Microscope	screws	McMaster Carr		#8-32 , 1inch long	1
Microscope	Open Cage box	Protolabs			1
Microscope	Galvo mount	Protolabs			1
Microscope	Window adapter	Protolabs			1
Microscope	Window plate	Protolabs			1
Microscope	motorized stage	Newport	UMR5XY-TRA12CC	Compact motorized linear stage, DC motor Q # 1004671	1
Microscope	stage driver	Newport	SMC100CC	Single-axis DC motor controller/driver	1
Microscope	stage power supply	Newport	SMC-PS80	Power Supply, SMC100 Series, 80W, 1	1
Microscope	stage interface	Newport	SMC-USB	USB Interface, Includes USB to COM Port Adapter & RS-232-C Cable, Windows	1

Appendix D

Control Box Components

	Component	Manufacturer	Manufacturer Part No.#	Description / comments
LAST UPDATE : 20120513				
Control Box Interface				
	Power Switch	NKK Switches	S301T	
	Enable Switch	NKK Switches	M2018SS1G03-RO	
	Laser Enable	NKK Switches	M2012SS1W01	
	Jog Switch	NKK Switches	M2011SS1W01	
	LED (115V)	Chicago Miniature	607-1050QC1	neon indicator
	LED (24V-red)	Chicago Miniature	1091M1-24V	
	LED (24V-green)	Chicago Miniature	1091M5-24V	
	T Sensor/Indicator	Lascar Electronics	EMT1900	Thermometer; 28 VDC; LCD; -20 degC to 220 degC (External Sensor); 1 degC; (LASCAR electronics# EMT1900)
	BNC	Amphenol	31-10-RFX	
	SMA	Amphenol	901-9889-RFX	
	USB	L-com Connectivity	ECF504-SC5E	
	80mm Fan	Orion Fans	OD8025-24HB	
	Power Cable Panel mount	Qualtek Electronics	701W-X2/04	
Power connection				
	Power Terminal 10p	Tyco Electronics	1-1546670-0	Connecting terminal block (double low)
	Power Terminal 6p	Tyco Electronics	1546670-6	Connecting terminal block (double low)
	Fan Power Supply	Tdk-Lambda	HK10-24/A	PWR SUP IND LOW PRO 24V .5A

	Component	Manufacturer	Manufacturer Part No.#	Description / comments
Cable assemblies				
	4 pin male	Tyco Electronics	794617-4	male = receptacle
	4 pin female (panel)	Tyco Electronics	794615-4	female = plug
	4 pin female (free)	Tyco Electronics	794616-4	
	20 pin male	Tyco Electronics	2-794617-0	
	20 pin female	Tyco Electronics	2-794615-0	
	20 pin female (free)	Tyco Electronics	2-794610-0	free hanging
	2 pin male	Tyco Electronics	1445022-2	
	2 pin female (panel)	Tyco Electronics	1445048-2	panel mount
	2 pin female (free)	Tyco Electronics	1445049-2	
	10 pin male	Tyco Electronics	1-1445022-0	
	10 pin female (panel)	Tyco Electronics	1-1445048-0	
	10 pin female (free)	Tyco Electronics	1-1445049-0	
	12 pin male	Tyco Electronics	1-1445022-2	
	12 pin female (panel)	Tyco Electronics	1-1445048-2	
	12 pin female (free)	Tyco Electronics	1-1445049-2	
	crimp male	Tyco Electronics	1-794612-1	
	crimp female	Tyco Electronics	1-794610-1	
	3 pin LDTC	Molex Connector Co	10-11-2103	for LDTC cable
	10 pin LDTC	Molex Connector Co	10-11-2103	for LDTC cable
	12 pin LDTC	Molex Connector Co	10-11-2123	for LDTC cable
	Molex crimp	Molex Connector Co	08-55-0129	for LDTC cable
	12 pin Copal cable	Nidec Copal Electronics		e-mail requested and were provided as free sample
	10 pin Copal cable	Nidec Copal Electronics		
Mechanical Layout				
	Standoff (1")	Keystone Electronics	8405	STDOFF HEX M/F 4-40 1.00"L ALUM
	Standoff (2")	Keystone Electronics	8412	STDOFF HEX M/F 4-40 2.00"L ALUM
	Standoff (1/4")	Keystone Electronics	8714	STDOFF HEX M/F 4-40 .250"L ALUM
	Standoff (1/4"-ff)	Keystone Electronics	2201	STANDOFF HEX 4-40THR ALUM .250"L
	heat sink	Crydom	HS301	
	galvo controller plate			custom designed
	slim posts (3")	New Port	SP-3	
	4-40 Nuts	B&F Fastener Supply	HNZ 440	4-40 NUT
	D-sub mount screws	Tyco Electronics	A32020-ND	FEMALE SCREW MOUNT
	D-sub mount screws	Tyco Electronics	5205980-4	MALE SCREW MOUNT
	Mating cable connectors	Tyco Electronics	1-794610-1	MATE-N-LOK 3MM RECP. CONTACT
	Mating cable connectors	Tyco Electronics	1-794612-1	MATE-N-LOK 3MM PLUG. CONTACT
	D-sub connector (15p) plug	Amphenol	L717SDA15P	CONN D-SUB PLUG 15POS GOLD FLASH
	D-sub connector (15p) receptacle	Amphenol	L77SDA15S	CONN D-SUB RCPT 15POS GOLD FLASH
	D-sub connector (9p) plug	Amphenol	L717SDE09P	CONN D-SUB PLUG 9POS GOLD FLASH
	D-sub connector (9p) receptacle	Amphenol	L77SDE09S	CONN D-SUB RCPT 9POS GOLD FLASH

Bibliography

[1] L An, J Qin, and R.K. Wang. Ultrahigh sensitive optical microangiography for in vivo imaging of microcirculations within human skin tissue beds. *Optics Express*, 18(8):8220–8228, 2010.

[2] Brett E Bouma and Guillermo J Tearney. *Handbook of Optical Coherence Tomography*. Informa Healthcare, 1st edition, November 2001.

[3] Brett E Bouma, Guillermo J Tearney, Benjamin J Vakoc, and Seok-Hyun Yun. *Biological and Medical Physics, Biomedical Engineering*. EliasGreenbaumBiological and Medical Physics, Biomedical Engineering1618-7210. Springer Berlin Heidelberg, Berlin, Heidelberg, 2008.

[4] Brett E Bouma, Seok-Hyun Yun, Benjamin J Vakoc, Melissa J Suter, and Guillermo J Tearney. Fourier-domain optical coherence tomography: recent advances toward clinical utility. *Current Opinion in Biotechnology*, 20(1):111–118, February 2009.

[5] Zhongping Chen, TE Milner, and X Wang. Optical Doppler Tomography: Imaging in vivo Blood Flow Dynamics Following Pharmacological Intervention and Photodynamic Therapy - Chen - 2008 - Photochemistry and Photobiology - Wiley Online Library. *Photochemistry and ...*, 1998.

[6] Gerd Häusler and Michael Walter Lindner. "Coherence Radar" and "Spectral Radar"—New Tools for Dermatological Diagnosis. *Journal of Biomedical Optics*, 3(1):21, January 1998.

[7] Menno Huikeshoven, Petra H L Koster, Corianne A J M de Borgie, Johan F Beek, Martin J C van Gemert, and Chantal M A M van der Horst. Redarkening of port-wine stains 10 years after pulsed-dye-laser treatment. *The New England journal of medicine*, 356(12):1235–1240, March 2007.

[8] Joseph A Izatt, Manish D Kulkarni, Siavash Yazdanfar, Jennifer K Barton, and Ashley J Welch. In vivo bidirectional color Doppler flow imaging of picoliter blood volumes using optical coherence tomography. *Optics Letters*, 22(18):1439–1441, 1997.

[9] Zaid F Jasim and Julian M Handley. Treatment of pulsed dye laser–resistant port wine stain birthmarks. *Journal of the American Academy of Dermatology*, 57(4):677–682, October 2007.

[10] Rainer A Leitgeb, Christoph K Hitzenberger, and A F Fercher. Performance of Fourier domain vs. time domain optical coherence tomography. *Opt. Express*, 11(8):889–894, 2003.

[11] F Lexer, Christoph K Hitzenberger, A F Fercher, and M Kulhavy. Wavelength-tuning interferometry of intraocular distances. *Applied Optics*, 36(25):6548–6553, September 1997.

[12] Adrian Mariampillai, Beau A Standish, Eduardo H Moriyama, Mamta Khurana, Nigel R Munce, Michael K K Leung, James Jiang, Alex Cable, Brian C Wilson, I Alex Vitkin, and Victor X D Yang. Speckle variance detection of microvasculature using swept-source optical coherence tomography. *Optics Letters*, 33(13):1530–1532, 2008.

[13] Wang-Yuhl Oh, Seok-Hyun Yun, and Guillermo J Tearney. 115 kHz tuning repetition rate ultrahigh-speed wavelength-swept semiconductor laser. *Optics Letters*, 2005.

[14] J M Smit, C G Bauland, D S Wijnberg, and P H M Spauwen. Pulsed dye laser treatment, a review of indications and outcome based on published trials. *British Journal of Plastic Surgery*, 58(7):981–987, October 2005.

[15] O.T. Tan, K Sherwood, and B.A. Gilchrest. Treatment of children with port-wine stains using the flashlamp-pulsed tunable dye laser. *New England Journal of Medicine*, 320(7):416–421, 1989.

[16] Benjamin J Vakoc, Ryan M Lanning, James A Tyrrell, Timothy P Padera, Lisa A Bartlett, Triantafyllos Stylianopoulos, Lance L Munn, Guillermo J Tearney, Dai Fukumura, Rakesh K Jain, and Brett E Bouma. Three-dimensional microscopy of the tumor microenvironment in vivo using optical frequency domain imaging. *Nature Medicine*, 15(10):1219–1223, September 2009.

[17] Ruikang K Wang, Steven L Jacques, Zhenhe Ma, Sawan Hurst, Stephen R Hanson, and Andras Gruber. Three dimensional optical angiography. *Optics Express*, 15(7):4083–4097, 2007.

[18] Seok-Hyun Yun, C Boudoux, Guillermo J Tearney, and Brett E Bouma. High-speed wavelength-swept semiconductor laser with a polygon-scanner-based wavelength filter. *Optics Letters*, 28(20):1981–1983, October 2003.

[19] Seok-Hyun Yun, Guillermo J Tearney, Johannes F de Boer, and Brett E Bouma. Removing the depth-degeneracy in optical frequency domain imaging with frequency shifting. *Optics Express*, 12(20):4822–4828, 2004.

[20] Seok-Hyun Yun, Guillermo J Tearney, Johannes F de Boer, N Iftimia, and Brett E Bouma. High-speed optical frequency-domain imaging. *Optics Express*, 11(22):2953–2963, November 2003.

[21] Y Zhao, K M Brecke, H Ren, Z Ding, J Stuart Nelson, and Zhongping Chen. Three-dimensional reconstruction of in vivo blood vessels in human skin using phase-resolved optical Doppler tomography. *IEEE Journal of Selected Topics in Quantum Electronics*, 7(6):931–935, 2001.

[22] Yonghua Zhao, Zhongping Chen, Christopher Saxer, Shaohua Xiang, Johannes F de Boer, and J Stuart Nelson. Phase-resolved optical coherence tomography and optical Doppler tomography for imaging blood flow in human skin with fast scanning speed and high velocity sensitivity. *Optics Letters*, 25(2):114–116, 2000.

[23] S Zotter, M Pircher, T Torzicky, M Bonesi, E. Götzinger, R.A. Leitgeb, and Christoph K Hitzenberger. Visualization of microvasculature by dual-beam phase-resolved Doppler optical coherence tomography. *Optics Express*, 19(2):1217–1227, 2011.